J. Fluid Mech. (2025), *vol.* 1009, A58, doi:10.1017/jfm.2025.204

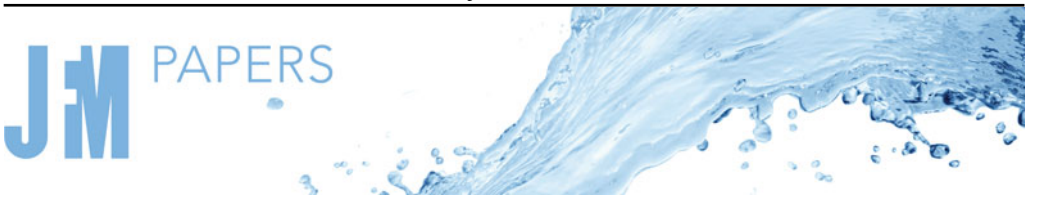

Stratified wake of a 6:1 prolate spheroid at a moderate pitch angle

Sheel Nidhan[1], **Sanidhya Jain**[1], **Jose Luis Ortiz-Tarin**[1] **and Sutanu Sarkar**[1]

[1]Department of Mechanical and Aerospace Engineering, University of California San Diego, La Jolla, CA 92093, USA

Corresponding author: Sutanu Sarkar, ssarkar@ucsd.edu

(Received 6 November 2024; revised 20 January 2025; accepted 31 January 2025)

The on-body flow and near-to-intermediate wake of a 6:1 prolate spheroid at a pitch angle of $\alpha = 10°$ and a length-based Reynolds number, $Re_L = U_\infty L/\nu = 3 \times 10^4$, are investigated using large eddy simulation (LES) across four stratification levels: $Fr = U_\infty/ND = \infty$, 6, 1.9 and 1. A streamwise vortex pair, characteristic of non-zero α in unstratified flow over both slender and blunt bodies, is observed. At $Fr = \infty$ (unstratified) and 6, the vortex pair has a lateral left–right asymmetry as has been reported in several previous studies of unstratified flow. However, at higher stratification levels of $Fr = 1.9$ and 1, this asymmetry disappears and there is a complex combination of body-shed vorticity that is affected by baroclinicity and vorticity associated with internal gravity waves. Even at the relatively weak stratification of $Fr = 6$, the wake is strongly influenced by buoyancy from the outset: (*a*) the vertical drift of the wake is more constrained at $Fr = 6$ than at $Fr = \infty$ throughout the domain; and (*b*) the streamwise vortex pair loses coherence by $x/D = 10$ in the $Fr = 6$ wake, unlike the $Fr = \infty$ case. For the $Fr = 1$ wake, flow separation characteristics differ significantly from those at $Fr = \infty$ and 6, resulting in a double-lobed wake topology that persists throughout the domain.

Key words: stratified flows

1. Introduction

1.1. *Slender body wakes in unstratified fluid at zero angle of attack*

The study of wakes behind slender bodies is a crucial area of fluid mechanics research with significant implications for various engineering applications. From the design of

This article has been updated since original publication. A notice detailing the change has also been published.

streamlined vehicles and structures to the understanding of biological locomotion, the behaviour of fluid flow in the wake region of elongated objects continues to present both challenges and opportunities. To the best of our knowledge, Chevray (1968) conducted the first experimental investigation of a slender body wake, employing a 6:1 prolate spheroid with a tripped boundary layer at an angle of attack $\alpha = 0°$ as the wake generator. Further experimental and computational studies by Jimenez *et al.* (2010), Posa & Balaras (2016) and Kumar & Mahesh (2018) have explored the on-body and near-wake dynamics of slender bodies at $\alpha = 0°$ and $Re_L \sim O(10^6)$, using the DARPA-SUBOFF with a tripped boundary layer (BL) as the wake generator. Due to limitations in the experimental set-up and the prohibitively expensive cost of performing wall-resolved simulations for slender bodies, these studies cover downstream distances of up to $x/D \approx 20$. In terms of the near wake, coherent vortex shedding was not detected. The absence of near-wake vortex shedding at a high Re_L with a tripped BL configuration was also found by Ortiz-Tarin *et al.* (2021) for a 6:1 prolate spheroid. This is in stark contrast to moderate- to low-Re_L configuration for slender bodies, 4:1 spheroid by Ortiz-Tarin *et al.* (2019) at $Re_L = 4 \times 10^4$ and 6:1 spheroid by Ohh & Spedding (2024), where clear vortex shedding from the slender wake generator is observed. It is worth noting that the high-Re spheroid wake of Ortiz-Tarin *et al.* (2021) at $Re_L = 6 \times 10^5$ exhibited a region where the flow evolved self-similarly but with a wake deficit law of $U_d \sim x^{-6/5}$ (different from the classical $U_d \sim x^{-2/3}$) due to non-equilibrium dissipation scaling (Nedić *et al.* 2013; Dairay *et al.* 2015) that has been attributed to unsteadiness in the energy cascade.

1.2. *Unstratified slender body wakes and streamwise vortices at non-zero pitch angle*

Another widely studied configuration involves unstratified flow past a spheroid, tilted at a non-zero pitch angle (α) relative to the incoming flow. While the separation region behind a slender body at $\alpha = 0°$ is relatively small compared with that of a bluff body, the separation patterns can change significantly as α increases. At even moderate angles of attack ($\alpha \in [10°, 20°]$), the separation line shifts upstream from the tail of the body and forms streamwise vortices on both sides as the flow detaches from the surface (Han & Patel 1979; Fu *et al.* 1994; Patel & Kim 1994). In addition to the primary streamwise vortices, secondary vortices with weaker circulation can also develop in these configurations (Fu *et al.* 1994).

The vortices shed off a slender body may not be axisymmetric even in the mean although the body is axisymmetric. The asymmetric nature of a slender-body wake at high angles of attack ($\alpha > 40°$) has been extensively documented for slender bodies with a sharp nose (Nelson & Pelletier 2003; Bridges 2006; Nelson *et al.* 2006). Direct numerical simulation (DNS) at moderate $Re_L \sim O(10^4)$ and high $\alpha = 45°$ (Jiang *et al.* 2015; Strandenes *et al.* 2019) for a 6:1 prolate spheroid reports that the flow separation, resulting wake and streamwise vortex pair are asymmetrical in the lateral direction, despite the configuration being symmetrical. This asymmetry induces a considerable lateral force on the spheroid. In the near wake, these studies do not find vortex shedding (Jiang *et al.* 2015). Instead, they report an asymmetric vortex pair where the vortex tube structure with larger circulation magnitude persists throughout the computational domain. At further higher $Re_L \sim O(10^6)$, DNS into the far wake becomes infeasible. Consequently, previous studies on flow past slender bodies at non-zero angle of attack have employed either Reynolds-averaged Navier–Stokes (RANS) simulations (Constantinescu *et al.* 2002) or large eddy simulations (LES) (Wikström *et al.* 2004; Plasseraud *et al.* 2023). These computational studies do not report any asymmetry in the flow separation or the resulting wake at $Re_L \sim O(10^6)$ and α within the range of 10°–20°.

The high-Re experimental study by Ashok *et al.* (2015*a*) does report asymmetry in the flow. The authors conducted detailed velocity measurements in the wake of a DARPA-SUBOFF model (an axisymmetric body) over a wide range of $Re_L \in [2.4 \times 10^6, 30 \times 10^6]$ at low to moderate angles of attack, up to $\alpha = 12°$. They observed that even at these low to moderate α values, the streamwise vortex pair and the wake structure were asymmetrical with the circulation of one vortex exceeding the other by 10 %–20 %. To assess the robustness of this asymmetry, they repeated their experiments under various conditions, such as changing the physical model and wind tunnel, and consistently found that the asymmetry remained a distinctive feature of the wake for such configurations. Some experimental studies (Grandemange *et al.* 2013; Rigas *et al.* 2014) have reported the presence of an asymmetric mode in bluff-body wakes, even at zero pitch and yaw. In these wakes, the time scale of the asymmetric mode is almost $O(10^2)-O(10^3)$ times larger than that of the vortex shedding mode.

1.3. *Stratification effects on slender-body wakes at zero pitch angle*

Despite their widespread use in naval and aerospace applications, the effect of stratification on slender-body wakes (Ortiz-Tarin *et al.* 2019, 2023; Ohh & Spedding 2024) is not as well studied as the effect of stratification on bluff bodies (Lin *et al.* 1992; Spedding *et al.* 1996; Spedding 1997; Dommermuth *et al.* 2002; Meunier & Spedding 2006; Brucker & Sarkar 2010; de Stadler & Sarkar 2012; Pal *et al.* 2017; Zhou & Diamessis 2019; Chongsiripinyo & Sarkar 2020; Rowe *et al.* 2020; Madison *et al.* 2022; Li *et al.* 2024). For a uniformly stratified medium, the effect of ambient stratification on the wake is quantified by the body-based Froude number, $Fr = U_\infty/ND$, where U_∞, N and D are the free stream velocity, buoyancy frequency and body length scale (diameter in the case of a sphere or disk and minor-axis diameter for a spheroid), respectively. The value of body Fr depends not only on the application through the submersible parameters (relative speed U and size D), but also strongly on the environment since N in s^{-1} can vary from 10^{-3} in the deep ocean to 10^{-2} in the upper ocean to values as large as 10^{-1} in a sharp pycnocline. $Fr = 1$ to 500 brackets most applications with lower values corresponding to low-speed operation of large vehicles or to ocean observation floats that have low relative velocity with respect to the background currents. Irrespective of the body Fr, the wake is inevitably affected by buoyancy since the progressive decrease (increase) of wake velocity (size) reduce the local Froude number to $O(1)$ and smaller. For bluff-body stratified wakes, a three-stage decay is well established: (*a*) 3-D regime with essentially unstratified wake behaviour until $Nt \sim O(1)$; (*b*) non-equilibrium (NEQ) regime from $Nt \approx 2-50$ where the defect velocity $U_d \sim x^{-0.25\pm0.04}$ and the wake continues to adjust to the buoyancy effects; and (*c*) quasi-two-dimensional (Q2-D) regime beyond $Nt \approx 50$, where $U_d \sim x^{-0.75}$ and wake organises progressively into horizontally meandering pancake vortices.

To the best of our knowledge, Ortiz-Tarin *et al.* (2019) was the first numerical study of the stratified flow past a slender body (4:1 spheroid) and it was conducted at a moderate Reynolds number $Re_L = 40\,000$. A major finding of their work is that the slender body exhibits stronger buoyancy effects at the same body-based Froude number (Fr) compared with a bluff body. For example, at a critical $Fr_c = \mathrm{AR}/\pi$, the flow separation past the spheroid is suppressed due to modulation by steady lee waves, leading to wake relaminarisation. Furthermore, even at $Fr = \infty$, representing the unstratified configuration, the wake and flow separation remain azimuthally symmetrical unlike its non-zero α counterparts (Ashok *et al.* 2015*a*; Jiang *et al.* 2015, 2016). They find that the topology of the separation line is strongly affected by the stratification level. Building upon this study, Ortiz-Tarin *et al.* (2023) studied the far wake of a prolate 6:1 spheroid at three different

stratification levels $Fr = \infty$, 10, 2, $\alpha = 0°$ and a higher $Re_L = 6 \times 10^5$. For a prolate 6:1 spheroid at $Fr = 2 \approx 6/\pi = Fr_c$, a strong effect of buoyancy on the mean wake is observed, causing the wake to transition to a Q2-D regime earlier than expected (at $Nt \approx 15$ instead of $Nt \approx 40 - 50$ for the sphere).

Apart from a recent experimental study (Ohh & Spedding 2024) of a spheroid at pitch in stratified flow, there is no other work reported on a stratified wake in this configuration. Ohh & Spedding (2024) use particle image velocimetry (PIV) to investigate $Fr \sim O(10)$ wakes at non-zero inclinations of $\theta = 10°$ and 20°. Notably, the pitched wake exhibited significant vertical displacement that was followed by an oscillatory return to its hydrostatic equilibrium position with a frequency of $2\pi/N$. Similar to the canonical straight-on flow, the spheroid at pitch exhibited a reduced decay rate of U_d and a reduced vertical wake extent (L_V) compared with its unstratified counterpart. The authors also reported lateral asymmetry in the streamwise shed vortices.

1.4. *Open questions and objectives of this study*

The previous subsections highlight a clear knowledge gap on the flow past slender bodies at non-zero angles of attack (α) in situations where the environment is stratified. The focus of the present work is on a 6:1 prolate spheroid at pitch angle α, where there is no comparable work apart from the PIV-based experimental study of a towed spheroid (Ohh & Spedding 2024). The present work, which is based on high-resolution (to be demonstrated shortly) LES, complements the previous experimental study. Apart from $Fr = 6$ that is close to their lowest $Fr = 8$ (converting from their R-based definition to our D-based Fr), our work considers more strongly stratified $Fr = O(1)$ wakes too. The near-body flow is also examined and the detailed database is interrogated to understand and quantitatively characterise buoyancy effects on the vortex wake that ensues when a slender body is in pitch.

Several questions are addressed as part of this work. (*a*) Is the notable vertical oscillation of the wake that was reported by Ohh & Spedding (2024) found in the present work? (*b*) How do the streamwise vortices, characteristic of inclined spheroids, and flow separation topology respond to buoyancy? (*c*) How do the mean fields for a spheroid at pitch evolve as a function of Fr, including the hitherto unreported $Fr = O(1)$ regime? (*d*) Does the lateral asymmetry in the streamwise vortex pair, previously observed at either small α with high Re_L (Ashok *et al.* 2015*a*) or large α with moderate Re_L (Jiang *et al.* 2015) under unstratified conditions, also occur at moderate α with moderate Re_L of the present unstratified case? (*f*) How do the characteristics of said asymmetry change with varying Fr – from unstratified to weak-stratification conditions of $Fr = 6$ to strongly stratified conditions of $Fr = 1.9$ and 1?

To this end, the paper is organised as follows. Section 2 details the numerical methods used and includes a study of grid quality. Section 3 presents an overall effect of buoyancy through flow visualisations at various Fr. Section 4 describes the evolution of the pressure coefficient (C_p) and friction coefficient (C_f) on the body, as well as flow separation. Sections 5 and 6 discuss the evolution of the mean wake (velocity and length scales) and the mean streamwise vorticity field, respectively. The study is concluded in § 7.

2. Methodology

2.1. *Governing equations and numerical scheme*

Figure 1 is a schematic of the simulation set-up wherein a 6:1 prolate spheroid, with major and minor axis given by $L = 6D$ and D, respectively, is placed at a pitch angle $\alpha = 10°$ in

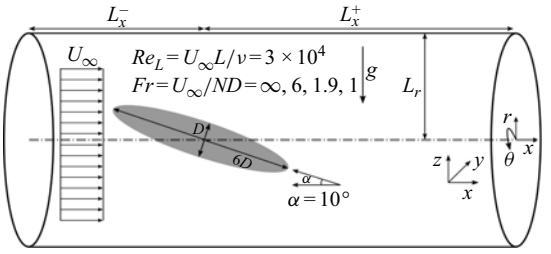

Figure 1. Schematic of the flow configuration that is simulated in a cylindrical domain (not to scale). L_x^-, L_x^+ and L_r refer to the upstream, downstream and radial domain distance, respectively. Re and Fr denote the minor-axis based Reynolds number and Froude number, respectively, and α is the pitch angle. Re_L is the major-axis based Reynolds number. The stratified cases correspond to a background with uniform thermal stratification. The centre of the spheroid is at the origin of the coordinate system.

a cylindrical computational domain. The background is thermally stratified with density variation inversely proportional to temperature variation. The non-dimensional filtered Navier–Stokes equations under the Boussinesq approximation, in conjunction with the continuity and density transport equation, are solved in a cylindrical coordinate system to simulate the flow past a prolate spheroid:

(i) continuity,

$$\frac{\partial u_i}{\partial x_i} = 0; \tag{2.1}$$

(ii) momentum,

$$\frac{\partial u_i}{\partial t} + \frac{\partial (u_i u_j)}{\partial x_j} = -\frac{\partial p}{\partial x_i} + \frac{1}{Re}\frac{\partial}{\partial x_j}\left[\left(1 + \frac{\nu_s}{\nu}\right)\frac{\partial u_i}{\partial x_j}\right] - \frac{1}{Fr^2}\rho_d \delta_{i3}; \tag{2.2}$$

(iii) density,

$$\frac{\partial \rho}{\partial t} + \frac{\partial (\rho u_j)}{\partial x_j} = \frac{1}{RePr}\frac{\partial}{\partial x_j}\left[\left(1 + \frac{\kappa_s}{\kappa}\right)\frac{\partial \rho}{\partial x_j}\right]. \tag{2.3}$$

Equations (2.1)–(2.3) are solved to obtain non-dimensional velocity u_i, density ρ and pressure p as the flow evolves. Following the Boussinesq approximation, ρ is decomposed as follows:

$$\rho(x_i, t) = \rho_0 + \rho_b(x_i) + \rho_d(x_i, t), \tag{2.4}$$

where ρ_0 corresponds to the base density, $\rho_b(x_i)$ is the background density variation and $\rho_d(x_i, t)$ is the density fluctuation. For linear stratification, $\partial \rho_b(x_i)/\partial z = C$, where C is a constant. Under the Boussinesq approximation, it is assumed that $\rho_b/\rho_0 << 1$ and $\rho_d/\rho_0 << 1$, which lead to the simplified continuity and momentum equations (2.1) and (2.2), respectively.

The non-dimensionalisation employs the following parameters: (i) free stream velocity U_∞ for u_i; (ii) minor axis length D for x_i; (iii) dynamic pressure $\rho_0 U_\infty^2$ for p; (iv) D/U_∞ for time t; (v) $-DC$ for density; (vi) kinematic viscosity ν for the subgrid kinematic viscosity ν_s; and (vii) molecular diffusivity κ for the subgrid molecular diffusivity κ_s. This non-dimensionalisation procedure results in the following non-dimensional parameters: (i) Reynolds number $Re = U_\infty D/\nu$; (ii) Froude number $Fr = U_\infty/(ND)$, where N represents the buoyancy frequency defined as $N = \sqrt{-gC/\rho_0}$; and (iii) Prandtl number $Pr = \nu/\kappa$. In this study, Re_L is fixed and Fr-based stratification (see table 1) is moderate

Case	Re_L	α	Fr	L_r/D	L_θ/D	L_x^-/D	L_x^+/D	N_r	N_θ	N_x
1	30 000	10°	∞	22	2π	12	48	718	256	2560
2	30 000	10°	6	53	2π	30	53	1000	128	3584
3	30 000	10°	1.9	53	2π	30	53	1000	128	3584
4	30 000	10°	1	53	2π	30	53	1000	128	3584

Table 1. Simulation parameters. N_r, N_θ, N_x correspond to the number of grid points in radial, azimuthal and streamwise directions, respectively. Here, Re_L and Fr are the major-axis Reynolds number and minor-axis-based Froude number, respectively.

($Fr = 6$), critical ($Fr = AR/\pi = 6/\pi \approx 1.9$) insofar as lee wave/wake interaction, and quite strong ($Fr = 1$). The Reynolds number $Re_L = U_\infty L/\nu$, which is based on the major axis and widely used in the literature on slender bodies, takes the value of 30 000. The pitch angle α is held constant at 10°. The Prandtl number is fixed at $Pr = 1$ for simplicity. For comparison, Pr is approximately 0.7 for temperature in air, 5–7 for temperature in water and 700 for salt in water.

The 6:1 prolate spheroid is represented in the computational domain using the immersed boundary method (IBM) as described by Balaras (2004) and Yang & Balaras (2006). The governing equations, as given in (2.1)–(2.3), are solved in cylindrical coordinates for the pressure (p), density (ρ) and the three velocity components (u_r, u_θ, u_x). Here, r, θ and x correspond to the radial, azimuthal and axial directions, respectively. These directions, along with the Cartesian coordinate system, are illustrated in figure 1. Spatial derivatives are calculated using second-order finite difference schemes, while temporal stepping is done using a fractional step method that combines the Crank–Nicolson method with a low-storage Runge–Kutta scheme (RKW3). In the predictor step, the pressure Poisson equation is solved using a direct solver (Rossi & Toivanen 1999). The kinematic subgrid viscosity (ν_s) and density diffusivity (κ_s) are determined using the dynamic Smagorinsky model (Germano *et al.* 1991). For a more detailed description of the stratified-flow solver employed in this study, interested readers are referred to Pal *et al.* (2017) and Chongsiripinyo & Sarkar (2020).

At the inlet, a uniform inlet velocity boundary condition is prescribed for the velocity components: $[u_x, u_r, u_\theta] = [U_\infty, 0, 0] = \mathbf{U}$. The outlet boundary condition for velocities corresponds to an Orlanski-type convective boundary condition (Orlanski 1976). The pressure p is set to zero at the inlet boundary. On the remaining boundaries (outlet and radial), a Neumann boundary condition is used for pressure. For stratified cases, a Robin boundary condition is applied at the radial boundary, satisfying $\partial\rho/\partial z = C$. This implies that the density far away from the wake generator is assumed to be unperturbed. On the body surface, a no-slip condition is prescribed for velocity, and the normal gradients of pressure and density are set to zero. To prevent the reflection of internal gravity waves from the boundaries, sponge layers are employed for velocity and density at the inlet, outlet and radial boundaries. These layers are defined as $\phi(x_i)(\mathbf{u} - \mathbf{U})$ for velocity components and $\phi(x_i)(\rho - \rho_b)$ for density, where ρ_b corresponds to the background density state. A quadratic damping function of the following form, $\phi(x_i) = C^*((x_i - x_{s,i})/(L_{x_i} - x_{s,i}))^2$, is used for the sponge. Here, $x_{s,i}$ is the start of the sponge layer and L_{x_i} is the extent of the numerical domain, respectively, in the ith coordinate axis direction. Additionally, $C^* = 10$ for $Fr = 1.9$ and 1 wakes and $C^* = 5$ for the $Fr = 6$ wake. For the unstratified wake, sponge layers are not necessary.

Flow statistics are obtained by time averaging with an averaging window of approximately two flow-through times $\approx 100D/U_\infty$. This time window is sufficient

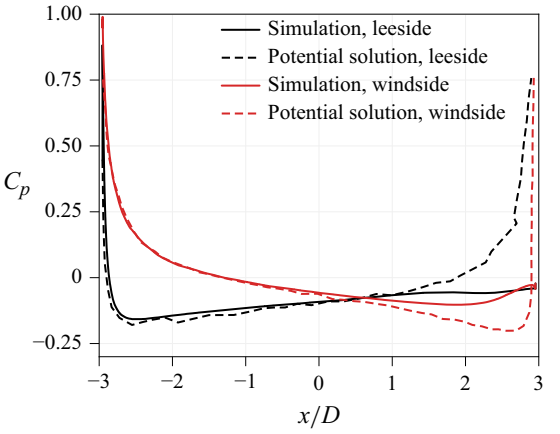

Figure 2. Variation of C_p in the $y/D = 0$ plane on the leeside and windside of the spheroid. Potential solution for C_p in dashed line, obtained from Piquet & Queutey (1992), is also shown.

for convergence of mean and second-order statistics of interest here. The time average (equivalent to ensemble or Reynolds average for this flow) is denoted by angle brackets, e.g. the average of u_x is $\langle u_x \rangle$. The simulations have approximately 458 million grid points for the stratified cases and 470 million grid points for the unstratified case (details given in § 2.2). These simulations were conducted on 128 or 256 CPUs, consuming approximately 500 000 compute hours for $150D/U_\infty$ simulation time units.

2.2. *Domain size and grid quality*

Table 1 presents the various grid parameters corresponding to the four simulations at $Fr = \infty$, 6, 1.9 and 1. The radial and upstream extent of the simulation domain, L_r and L_x^-, respectively, is increased for the stratified simulations to ensure that the steady lee waves weaken before they hit the radial and upstream boundary. Additionally, the azimuthal grid points in the unstratified $Fr = \infty$ simulation is increased to $N_\theta = 256$ from $N_\theta = 128$ in the stratified cases. The increased vertical displacement of the $Fr = \infty$ wake (figure 13*b*) to higher-r regions requires a smaller azimuthal grid spacing ($2\pi r/N_\theta$) and thus larger N_θ to ensure adequate azimuthal resolution away from the centreline.

For stratified wakes, the minimum $\Delta r/D \approx 7 \times 10^{-4}$ occurs at $r/D \approx 0$ and remains approximately constant until $r/D \approx 0.8$. Beyond this point, the radial grid is stretched until the edge of the radial domain. In the streamwise direction, the minimum $\Delta x/D = 4 \times 10^{-4}$ occurs at the nose of the spheroid. The streamwise grid is gradually stretched, due to the thickening of the boundary layer, reaching $\Delta x/D \approx 7 \times 10^{-3}$ at the tail. The stratified simulations were conducted prior to the unstratified simulations and it was found that the minimum $\Delta r/D$ could be relaxed. Therefore, in the unstratified case, $\Delta r/D \approx 2 \times 10^{-3}$. Aside from this adjustment, the grid distribution over the body remains the same as in the stratified case. At $x/D = 0$, at the centre of the spheroid, there are approximately 40–50 grid points across the δ_{99} thickness of the BL on the leeside of the spheroid for stratified cases. For the unstratified case, this number is ~ 22. At the tail of the spheroid, there are 90 points and 47 points across the δ_{99} thickness of BL for $Fr = 6$ and ∞, respectively.

Figure 2 shows a comparison between the $Fr = \infty$ simulation and the potential flow solution for the coefficient of pressure, $C_p = (P - P_\infty)/0.5\rho U_\infty^2$. The match between the potential solution and the current simulation is excellent until $x/D \approx 1$, indicating sufficient grid resolution to capture the boundary-layer evolution. Beyond $x/D \approx 1$, pressure recovery does not happen in our simulation due to viscous effects and subsequent

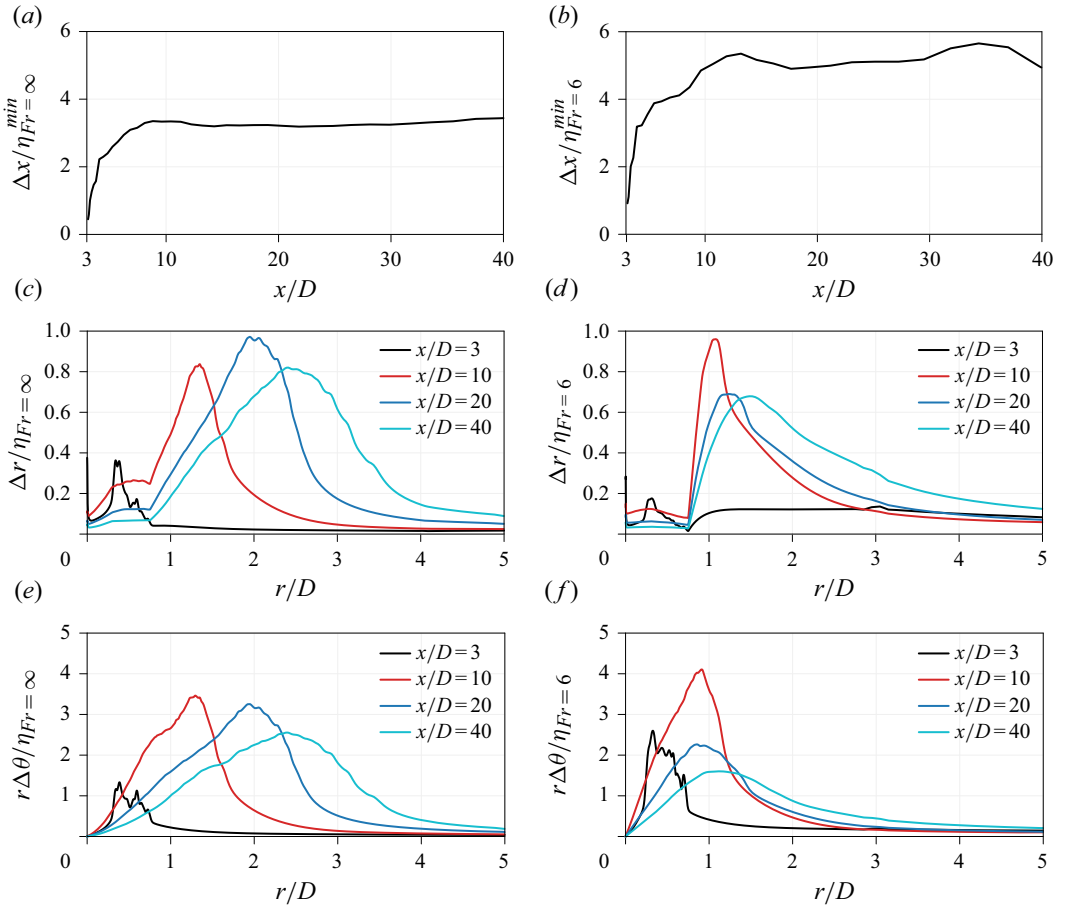

Figure 3. Ratio of grid size to Kolmogorov length η in all three directions for (a,c,e) $Fr=\infty$ and (b,d,f) $Fr=6$. For panel $(a,\ b)$, the smallest η at the corresponding x/D is used for calculation. For panel $(c-f)$, dissipation along the line $\theta=3\pi/2$ is used at respective x/D locations, since wake descends as it evolves.

boundary-layer separation. Here, C_p for the $Fr=6$ case is very similar to the unstratified case and is not presented for brevity.

To assess grid quality in the wake, the spatial variation of the ratio of grid spacing to the Kolmogorov length, denoted as $\eta=(\nu^3/\varepsilon)^{1/4}$, is computed in all three directions and shown in figure 3. We present results for $Fr=\infty$ and 6, specifically, for two reasons: (a) distinct grid resolutions for the unstratified and stratified cases (refer to table 1); and (b) the relatively strongly stratified simulations at $Fr=1$ and 1.9 are less turbulent than $Fr=6$ at $Re_L=30\,000$, and hence have better resolution of the wake turbulence. Figure 3 shows that the ratios of streamwise (Δx), radial (Δr) and azimuthal $(r\Delta\theta)$ grid spacing to η stay below 6, 1 and 5, respectively, for both $Fr=\infty$ and 6, establishing that the current LES study has been conducted at high resolution. The Ozmidov scale, $L_O=\sqrt{\varepsilon/N^3}$, is also well resolved with $\Delta r/L_o<0.1$ in the turbulent wake.

3. Visualisations

Isovolumes for instantaneous axial velocity (u_x) for all Fr are shown in figure 4. These visualisations provide insights into buoyancy effects on the wake structure before moving

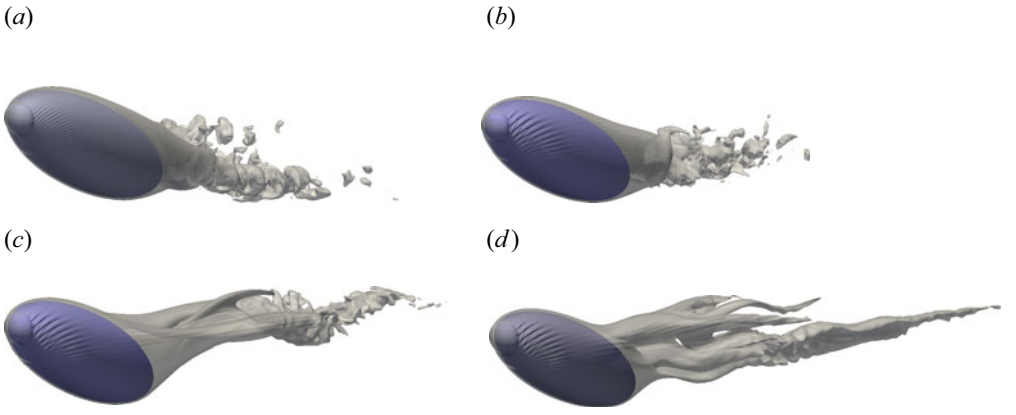

Figure 4. Instantaneous axial velocity (u_x) isovolumes: (*a*) $Fr = \infty$; (*b*) $Fr = 6$; (*c*) $Fr = 1.9$; and (*d*) $Fr = 1$, with maximum value of $u_x/U_\infty = 0.75$ and viewed from the front-left of the body.

on to quantification through mean velocity and vorticity fields in later sections. It is evident that, as Fr decreases, the topology of flow separation is altered and there is a systematic decrease in wake turbulence. It is also worth noting that, using finer azimuthal grid size, the streak-like ripples in figure 4 have been confirmed to be mere artefacts of visualisation in Paraview and should not be misconstrued as a physical phenomenon.

For the $Fr = \infty$ wake, two lobes of velocity defect are seen – one for each side of the body (figure 4*a*). These lobes break up quickly (at $x/D \approx 5$) into multiscale structures, implying transition from the initially laminar separation. Similar multiscale structures are observed in the $Fr = 6$ wake (figure 4*b*), but the breakup is observed further downstream ($x/D \approx 10$) relative to $Fr = \infty$. The wakes at higher stratification ($Fr = 1.9$ and $Fr = 1$) are significantly different. Although, two velocity defect lobes can also be seen in the $Fr = 1.9$ wake (figure 4*c*), they do not transition to smaller-scale structures until much further downstream ($x/D \approx 20$). At $Fr = 1$, transition to turbulence is further inhibited by buoyancy and the wake stays laminar throughout with a layered structure. Furthermore, two vertically separated and distinct regions of flow separation are observed at $Fr = 1$. These distinct regions have an imprint on wake evolution as will be quantified later.

Figure 5 presents another view of u_x-isovolumes, this time with streamlines added. With this view, the two lobes of the $Fr = \infty$ wake are seen to break down into spiral structures (figure 5*a*). Additionally, it is apparent that the unstratified wake descends vertically. The streamlines indicate cross-flow from the windward side towards the leeward side at all stratification levels. A similar spiral structure is observed in the $Fr = 6$ wake (figure 5*b*). However, less vertical drift is observed as will be quantified later. Once again, the $Fr = 1.9$ and $Fr = 1$ wakes exhibit notable differences from the wakes at higher Fr. While two structures emerge from either side of the body at $Fr = 1.9$ (figure 5*c*), akin to previous cases, large-scale undulations are observed in the isovolume and the streamlines due to the lee-waves-induced wake oscillation that has been previously reported for cases without angle of attack. Furthermore, the cross-flow from windward to leeward sides that was observed in the streamlines of the previous cases is now mildly suppressed at $Fr = 1.9$ and even more so at $Fr = 1$ (figure 5*d*). Moreover, the lee-waves-induced oscillations of the wake are stronger at the lower values of Fr.

The influence of stabilising buoyancy on the cross-flow and the resulting wake structure is made clearer by visualising streamlines of the secondary flow on a cross-section perpendicular to the inclined major axis of the body in figure 6. Contours of vertical

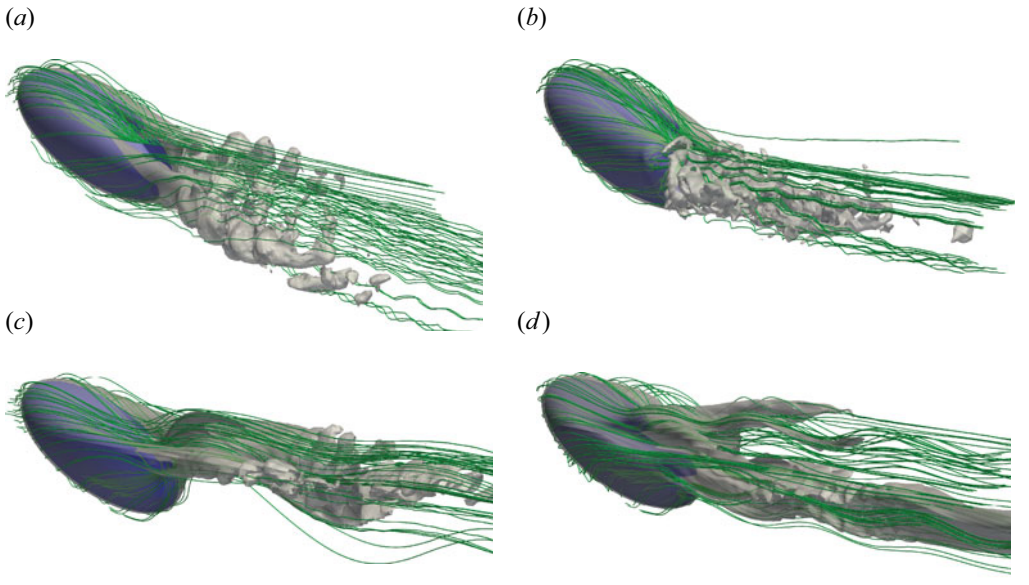

Figure 5. Instantaneous axial velocity (u_x) isovolumes along with streamlines: (*a*) $Fr = \infty$; (*b*) $Fr = 6$; (*c*) $Fr = 1.9$; and (*d*) $Fr = 1$. The isovolumes correspond to $u_x/U_\infty \leqslant 0.75$ and are viewed from the rear-left of the body.

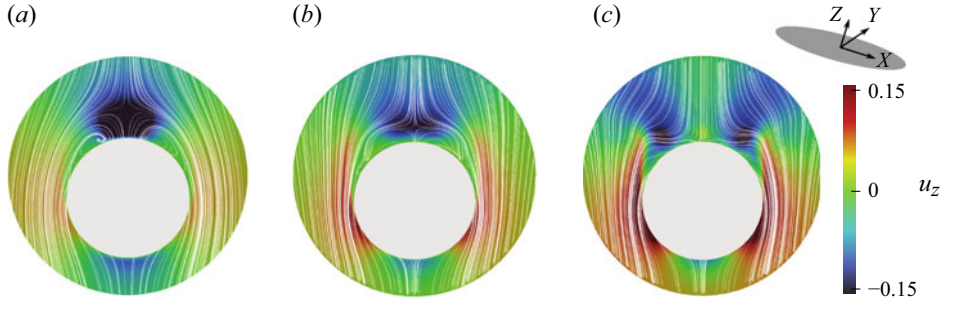

Figure 6. Streamlines of the secondary flow on a domain cross-section at $X/D = 1$ with normal as the major axis of the body. The bottom half of each panel corresponds to the windward side of the spheroid at $\alpha = 10°$. Contours of the vertical velocity (u_z) are shown: (*a*) $Fr = \infty$; (*b*) $Fr = 1.9$; and (*c*) $Fr = 1$. Here, X is the coordinate along the major axis of the body, where $X = 0$ corresponds to the centre of the body. The contours are in the $Y-Z$ plane normal to the major axis of the body. Top-right inset shows the (X, Y, Z) coordinate system.

velocity (u_z) are also depicted. Note that the cross-sections shown in figure 6 are in the plane normal to the major-axis of the body. In the case of $Fr = \infty$, the cross-flow is conspicuous, with the flow curving as it moves from the windward side to the leeward side (figure 6*a*). Atop the body, there is an attached circulation zone with two oppositely rotating streamwise vortices on either side. The imprint of stratification begins to manifest at $Fr = 1.9$ as follows: (*a*) streamlines that show flattening of the attached recirculation zone (figure 6*b*); and (*b*) u_z contours that show a higher upward velocity at the sides, whereas the downward velocity diminishes at the top. These features can be attributed to buoyancy whereby lighter fluid that is brought downward on the windward side by the inclined spheroid tends to rise to its neutral position and then

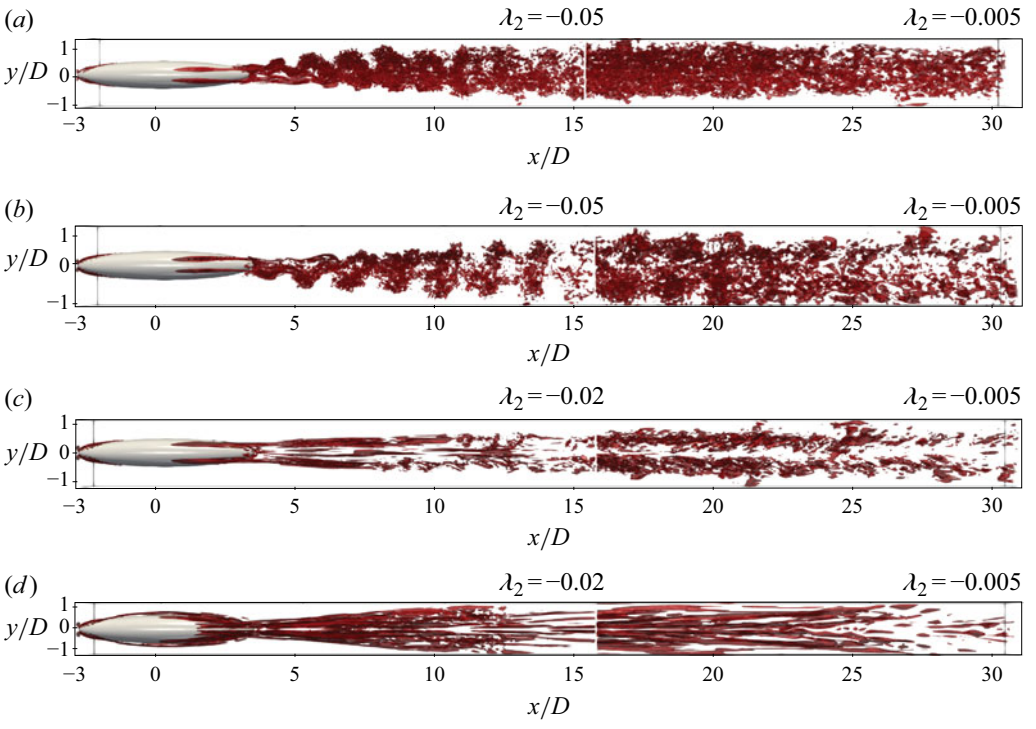

Figure 7. Isocontours for λ_2 criterion (top-view) are shown: (*a*) $Fr = \infty$; (*b*) $Fr = 6$; (*c*) $Fr = 1.9$; and (*d*) $Fr = 1$. Contour levels for each case are mentioned on top of each panel.

cannot curve downward across isopycnals. These effects become even more pronounced at $Fr = 1$, where the secondary-flow pattern (figure 6*c*) changes: the secondary streamlines rise almost vertically from the windward side before traversing almost horizontally to the leeward side along isopycnals. Consequently, some of the $Fr = 1$ flow separates prematurely from the top, as will be shown quantitatively through the skin friction. This region of separated flow – a secondary wake – remains distinct from the primary wake formed after the flow separates further downstream, as observed in figures 4(*d*) and 5(*d*).

To visualise vortical flow structures, isocontours of the λ_2 criterion are shown in figure 7. For all four cases, the isocontour threshold at $x/D \gtrapprox 15$ is smaller than at $x/D \lessapprox 15$ to ensure similar visibility between the near and intermediate wake. For $Fr = \infty$ and 6 (figure 7*a,b*), there is a distinct signature of a helical vortical structure developing from each lateral side of the body. These structures stay asymmetrical in the spanwise direction, a phenomenon consistent with the asymmetry previously observed in the velocity field (figures 4 and 5) and will be discussed further in the following sections. Coherent vortical structures become difficult to distinguish from small-scale turbulence when $x/D \gtrapprox 15$. At the higher stratification of $Fr = 1.9$ and 1 (figure 7*c,d*), layering of the instantaneous λ_2 isocontours is observed in the near wake with no distinguishable helical structures. These layers subsequently break down into small-scale structures as the wake evolves.

4. Body forces

At $\alpha = 0$, the buoyancy force affects the acceleration/deceleration of the flow through its tangential component and, through its normal component, influences the confinement of the boundary layer. The steady lee wave also imposes its pressure gradient and velocity

on the boundary layer. In addition, at $Fr \leqslant 1$, the fluid tends to move sideways instead of over and below the body, owing to the potential energy barrier imposed by the stable stratification. These effects of buoyancy on the force coefficients, the boundary-layer structure and its separation at $\alpha = 0°$, which were described in detail by Ortiz-Tarin *et al.* (2019) for a straight-on 4:1 spheroid, are also operative at a non-zero pitch angle. Importantly, for a pitched spheroid, there is an additional consequence of buoyancy whereby it influences the cross-flow and secondary circulation, as will be shown in this section.

Body forces are diagnosed by (*a*) the streamwise variation of pressure and shear-stress on the lee and windside as contour plots and (*b*) the streamwise variation of the force coefficients (C_p and C_f) along the body surface in the central plane ($y = 0$) as line plots. Here, $C_p = (P - P_\infty)/0.5\rho U_\infty^2$ and $C_f = Re^{0.5}|\tau_x|/0.5\rho U_\infty^2$. It is found that the previously noted buoyancy effects on the flow are strongly reflected by differences in the streamwise variation of body forces among the different stratification levels. A summary of these differences follows.

4.1. *Pressure coefficient*

Figure 8(*a,c,e,g*) shows the pressure contours on the leeside and figure 8(*b,d,f,h*) shows those on the windside of the body. The streamwise variation of C_p in the centreplane ($y = 0$) on both lee and windside is shown in figure 8(*i,j*) and is discussed first. For comparison, C_p obtained from the potential-flow solution (Piquet & Queutey 1992) is also presented in figure 8(*i,j*). For both sides, LES solutions agree well with the potential solution till $x/D \approx 1$, beyond which they deviate from the potential-flow solution owing to viscous effects and subsequent flow separation. On both sides, C_p rapidly drops from its stagnation value near the nose of the body. The value of this initial drop of C_p decreases systematically from its largest value at $Fr = \infty$ as Fr decreases (figure 8*i*).

On the leeside, the initial drop in pressure near the nose is followed by a slow and continuous recovery that is similar among the $Fr \geqslant 1.9$ cases (figure 8*i*). In contrast, at $Fr = 1$, the pressure recovery on the lee side does not occur until $x/D \approx 1.5$ so that the front part of the body ($x/D < 0$) has higher pressure than the other cases, which is a contributor to the increased drag in this case. The delayed pressure recovery can be observed both from the pressure contours (figure 8*g*) and the C_p evolution at the centreline (figure 8*i*). Mean pressure contours in the vicinity of the spheroid (not shown here for brevity), reveal a strong low-pressure region on the entirety of the leeside. This low-pressure region is imposed by the strong steady lee wave field at $Fr = 1$. It can also be seen that the leeside pressure contours for $Fr = \infty$ and 6 (figure 8*a,c*) show lateral asymmetry about the centreline ($y = 0$), which is consistent with the results of the previous section. The windside of the body exhibits more pronounced differences between unstratified ($Fr = \infty$) and strongly stratified ($Fr = 1.9, 1$) cases as compared with the leeside. Here, C_p of $Fr = 1.9$ and 1 falls significantly below those of $Fr = \infty$ and 6 after $x/D \approx 2$, and recovers sharply towards the end of the body. Pressure contours in figure 8(*b,d,f,h*) confirm this trend of higher and lower pressure at the nose and the tail of the body, respectively, for the $Fr = 1$ and 1.9 cases compared with the $Fr = 6$ and ∞ cases.

4.2. *Friction coefficient*

Figure 9(*a,c,e,g*) displays the scaled shear stress contours, $Re^{0.5}|\tau_x|$, on the leeside (left) and figure 9(*b,d,f,h*) those on the windside of the body across all Fr. These contours reveal that flow separation primarily occurs on the leeside, identifiable by regions in green where $|\tau_x| \to 0$. For the unstratified ($Fr = \infty$) and weakly stratified ($Fr = 6$) cases, the wake

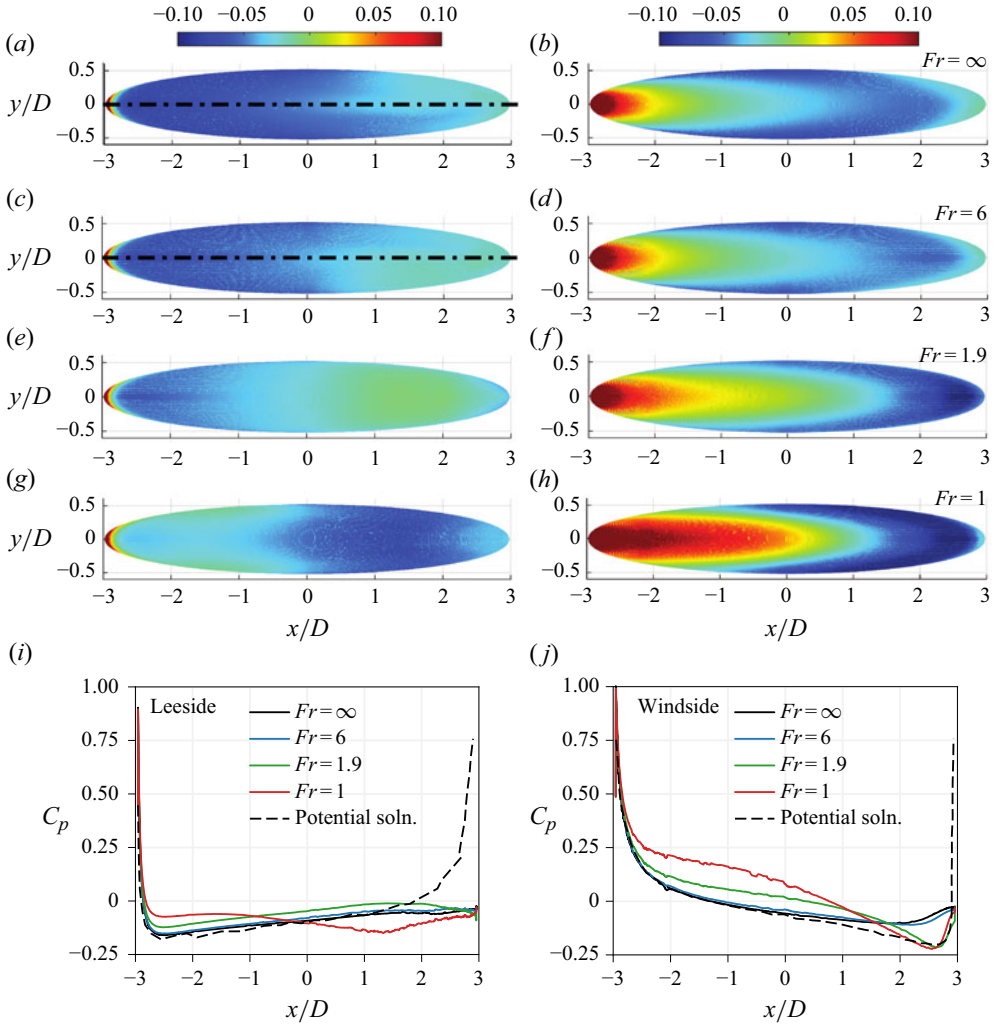

Figure 8. Pressure contours on the (*a,c,e,g*) leeside and (*b,d,f,h*) windside of the spheroid. Dashed line in panels (*a*) and (*c*) corresponds to $y/D = 0$. Variation of $C_p(x)$ on the (*i*) leeside and (*j*) windside of the body surface in the $y/D = 0$ plane. The potential flow solution for $C_p(x)$, obtained from Piquet & Queutey (1992), is also shown as a dashed line in panels (*i*) and (*j*).

separates mainly from the lateral portions of the leeside (figure 9*a*,*c*), forming a streamwise vortex pair to be discussed in § 6.

A central region (in red) near $y = 0$ remains attached until nearly the tail, with a noticeable lateral asymmetry. At $Fr = 1.9$, separation occurs both from the sides and the central region around $y = 0$ (figure 9*e*). However, at $Fr = 1$, separation is primarily central, with no clear lateral separation (figure 9*g*). Recall that a distinct streamwise vortex pair was present at $Fr = 1.9$ (figure 7*c*) but, at $Fr = 1$, the vortex pair is less evident.

The variation of C_f on the body surface at the $y = 0$ plane is shown in figure 9(*i*,*j*). For all cases, C_f varies quite similarly on both sides till $x/D \approx 0$. For $x \geqslant 0$, $Fr = \infty$ and 6 show higher C_f on the leeside (figure 9*i*) than their strongly stratified counterparts of $Fr = 1.9$ and 1. On the windside, $Fr \leqslant 1.9$ cases show elevated levels of C_f when compared with $Fr \geqslant 6$ cases (figure 9*j*). This region of elevated surface shear in

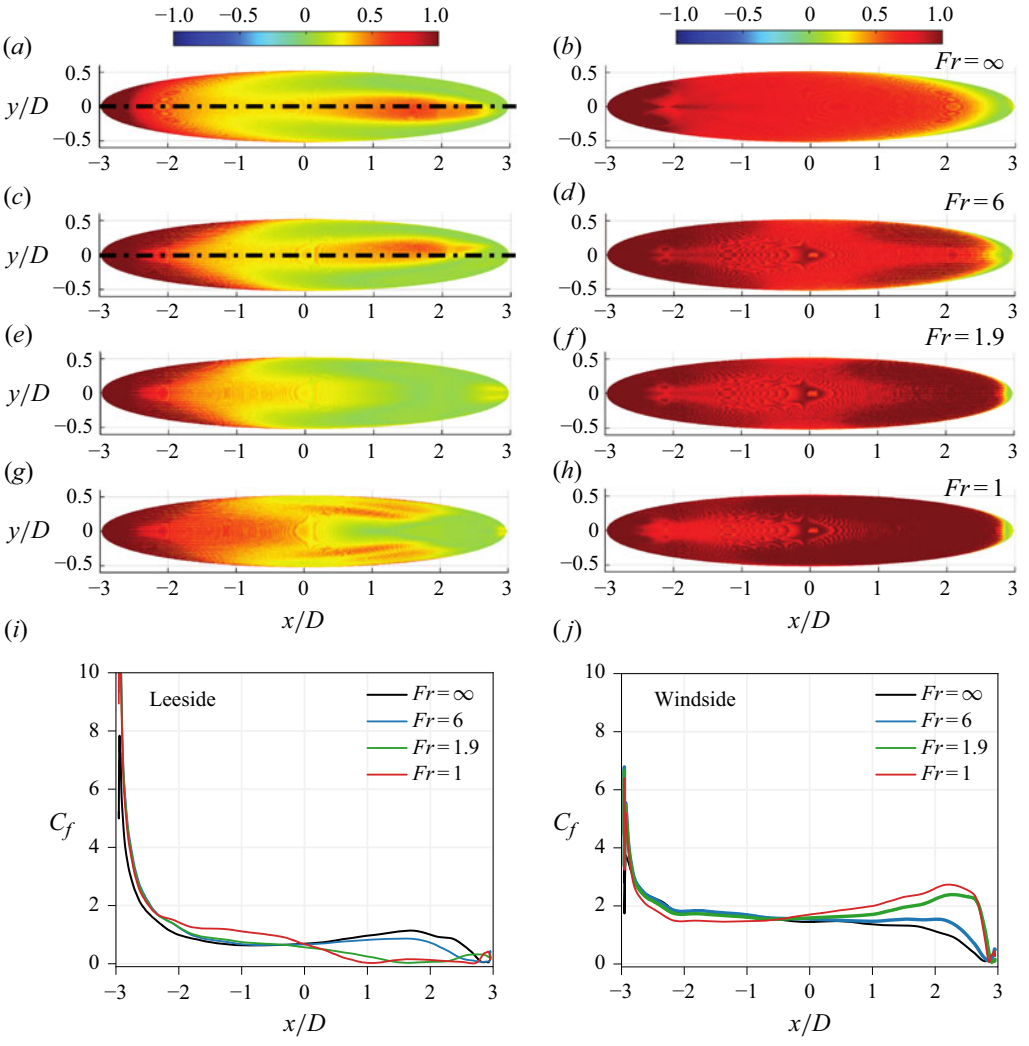

Figure 9. Contours of $Re^{0.5}|\tau_x|$ on the (*a,c,e,g*) leeside and (*b,d,f,h*) windside of the spheroid for all Fr at $\alpha = 10°$. Dashed lines in panels (*a*) and (*c*) correspond to $y/D = 0$. Variation of C_f on the (*i*) leeside and (*j*) windside of the body at the $y/D = 0$ plane.

$Fr = 1.9$ and $Fr = 1$ coincides with the region of steep pressure drop observed at $x/D > 1$ (figure 8*j*). The elevated surface shear is related to an accelerating external flow that thins the boundary layer.

4.3. *Overall forces*

The aforementioned changes in C_p and C_f lead to a buoyancy effect on overall drag. Also, in cases with lateral asymmetry, there is an additional sideways force. Since the flow separation and the boundary layer developing over the body remain laminar at $Re_L = 30\,000$, the fluctuation root mean square (r.m.s.) of force coefficients is negligible. Hence, only mean force coefficients are discussed in this section.

Figure 10 shows the drag $C_d = F_x/(1/2\rho U_\infty^2 A)$ and spanwise force $C_y = F_y/(1/2\rho U_\infty^2 A)$ coefficients as well as their partition into pressure and frictional

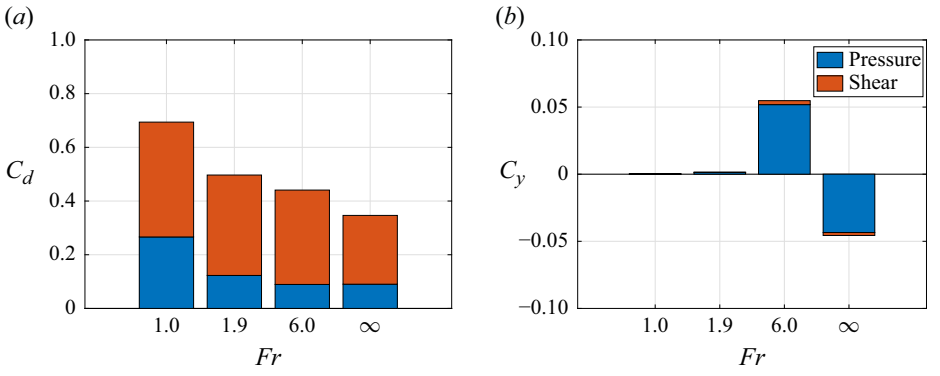

Figure 10. Force coefficients decomposed between pressure and shear contribution. Coefficient of (*a*) drag (C_d) and (*b*) lateral force coefficient (C_y).

coefficients. Here, $A = \pi D^2/4$. Additionally, C_d exhibits a systematic and moderate increase as stratification increases until $Fr = 1.9$. At $Fr = 1$, there is a relatively larger increase in C_d. The increased drag at $Fr = 1$ is primarily associated with a rise in the pressure contribution that is a consequence of the extended zone of high pressure on the windside that is seen at $Fr = 1$ (figure 8*i*) and not in the other cases.

Figure 10(*b*) shows the dependence of the lateral force coefficient (C_y) on stratification. The weakly stratified ($Fr = 6$) and unstratified ($Fr = \infty$) flow exhibit a sideways force consistent with the previously noted lateral asymmetry of C_p and C_f distributions. It is worth noting that the C_y of $Fr = \infty$ and $Fr = 6$ are similar in magnitude but flipped in sign. We hypothesise that the $Fr = \infty$ and $Fr = 6$ flows are bi-stable with two different reflectional-symmetry-breaking states, each state being equally probable. The lower $Fr = 1.9$ and 1 cases do not show asymmetry (associated with one streamwise vortex being larger than its partner) since buoyancy changes the cross-flow secondary circulation strongly (figure 6) to inhibit the rollup into streamwise vortices. Corresponding to the lateral symmetry, $C_y \approx 0$ for these cases.

5. Mean velocity and geometry of the wake

The variation of mean defect velocity, $U_\infty - \langle u_x(x, y, z)\rangle$, hereafter denoted by U_d, as a function of Fr is of interest. Buoyancy effects that alter the flow at the body and its separation were discussed in §§ 3 and 4, and are manifested as persistent differences in the near wake. These differences in the near wake and those in the far wake are elaborated below. The streamwise evolution will be presented as a function of x/D, where x is measured from the centre of the body. Buoyancy time, $Nt = Nx/U_\infty = (x/D)/Fr$, which is often used to gauge the strength of buoyancy effects, will also be used to discuss results as appropriate.

5.1. *Evolution of mean velocity on streamwise-constant planes*

Figure 11 presents mean defect velocity U_d contours at various streamwise locations ($x/D = 3$, 10, 20 and 30). In stratified scenarios, mean isopycnals are superimposed on the U_d contours. In the $Fr = \infty$ unstratified wake, two distinct lobes are evident as the flow leaves the body at $x/D \approx 3$ (figure 11*a*). These lobes are also observable in the instantaneous visualisations of $Fr = \infty$ (figure 5*a*). The asymmetry of flow at the body and its separation persist downstream leading to the asymmetry in $U_d(y, z)$ profiles between

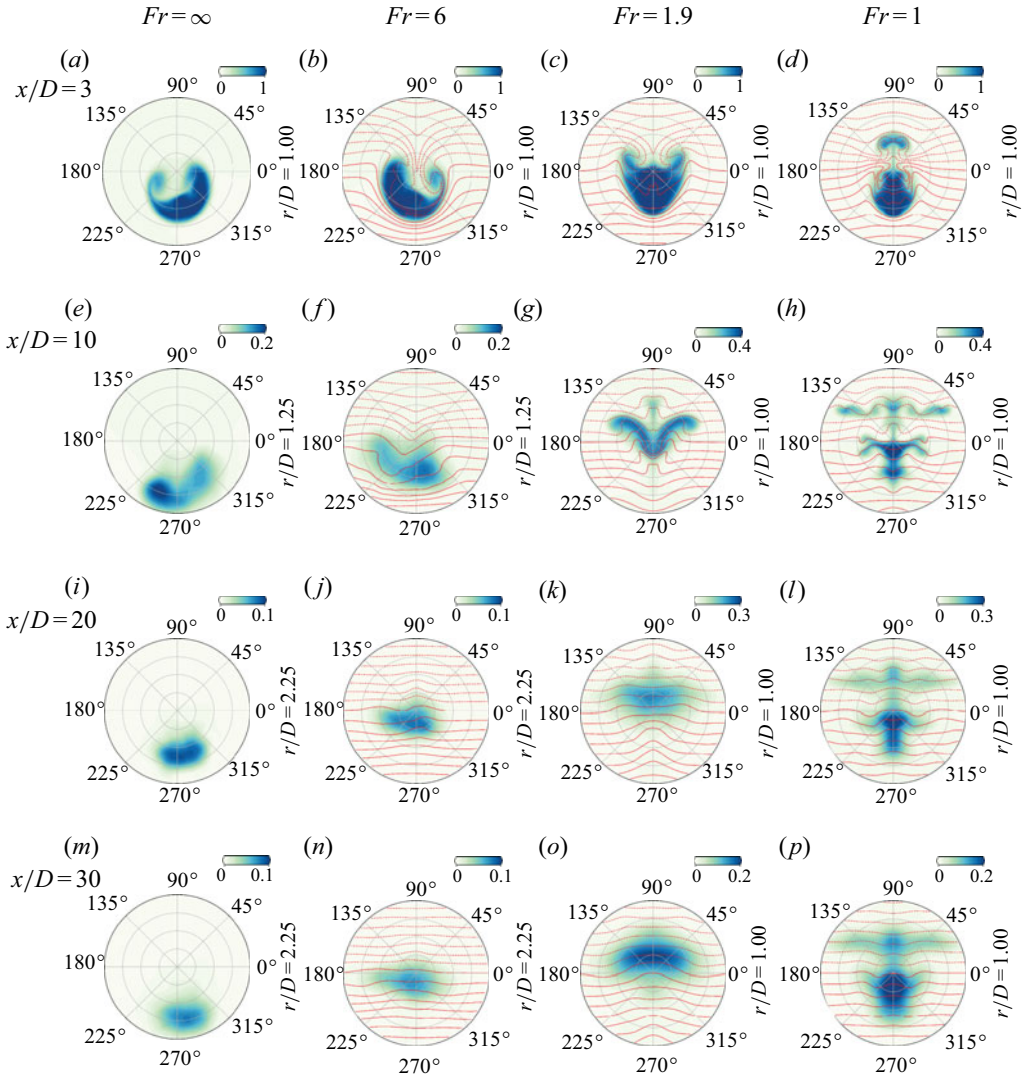

Figure 11. Mean defect velocity (U_d) contours and isopycnals at $x/D = 3$, 10, 20 and 30 (row-wise) for $Fr = \infty$, 6, 1.9 and 1 (column-wise). The extent of the radial domain is shown adjacent to each contour plot. For the stratified cases, body-generated steady lee waves in the domain are not visible due to the choice of contour ranges to focus specifically on the wake defect.

the left and right lobes. Asymmetric flow separation also occurs for $Fr = 6$, but with the direction of asymmetry reversed. No preferred direction for lateral asymmetry has been imposed by us; however, small asymmetries in the evolving flow have resulted in the observed polarity of the asymmetry. The asymmetry observed in the $Fr = \infty$ wake persists until at least $x/D = 10$ (figure 11*e*). However, by $x/D = 20$, the U_d contours for the $Fr = \infty$ case no longer exhibit the distinct lobes observed in the near wake. Another noteworthy observation is the continuous drift of the U_d contour in both the vertical (z) and spanwise (y) directions due to the body's angle of inclination and the wake's asymmetry, respectively. These vertical and horizontal drifts will be further quantified in subsequent sections of the manuscript.

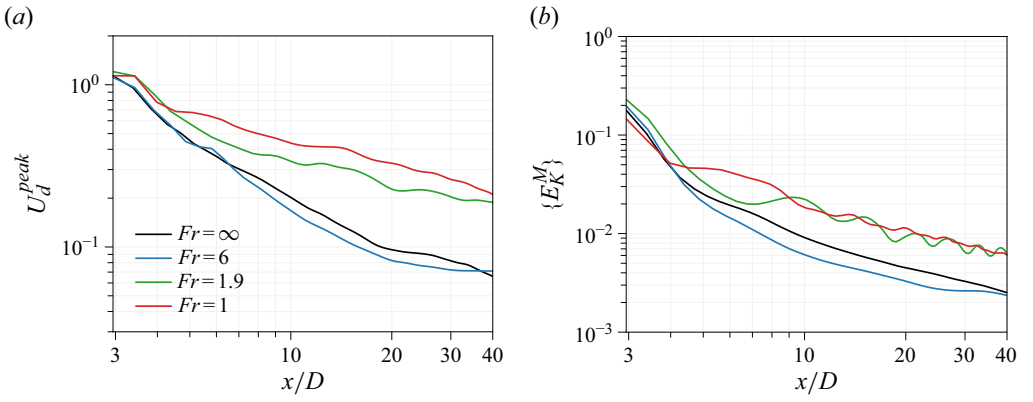

Figure 12. (*a*) Decay of the mean defect velocity peak, U_d^{peak} and (*b*) area-integrated mean kinetic energy, $\{E_K^M\}$, decay for different Fr.

Despite its weak stratification, the evolution of the $Fr = 6$ wake is affected early on. At $x/D = 10$ or $Nt = 1.67$ (figure 11*g*), its vertical downward displacement is significantly less than in the unstratified case. The lower boundary of the wake is seen to lie along one of the isopycnals displaced by the flow. The restoring force of buoyancy comes into play so that, with the downstream weakening of the wake deficit and the associated recovery of the boundary isopycnal to its neutral position, the mean wake tends to return towards the centreline ($z = 0$).

In the strongly stratified cases of $Fr = 1.9$ and 1, the mean flow leaving the body is no longer laterally asymmetric, as seen in figure 11(*c*,*d*). It was shown previously that the sideways force coefficient (C_y) approaches zero at $Fr = 1.9$ and $Fr = 1$ (figure 10*b*). Similar to the $Fr = \infty$ and $Fr = 6$ cases, most of the wake at $x/D = 3$ is below the $z = 0$ plane for both $Fr = 1.9$ and 1. Similar to the $Fr = 6$ wake, the $Fr = 1.9$ wake and its corresponding isopycnals are constrained by the restoring force of buoyancy, which is stronger and is manifested as lee-waves-induced oscillations as the wake progresses downstream. By $x/D = 30$ (figure 11*o*), an elliptical U_d topology appears for the $Fr = 1.9$ wake.

The downstream evolution of the $Fr = 1$ wake differs significantly from the other three cases. Immediately after the body, the wake assumes a double-lobed structure with isopycnals extending both upward and downward. These two lobes evolve independently of each other. By $x/D = 30$, the $Fr = 1$ wake has a significantly greater vertical extent than the $Fr = 1.9$ wake due to the initial emergence and persistence of the double-lobed structure, which eventually transitions into a double-layered wake, as shown in figure 11(*p*). The upper lobe – a secondary wake – originates from the region of separated flow from the top, recall the discussion of figure 9(*g*).

5.2. *Evolution of peak defect velocity and mean kinetic energy*

Figure 12(*a*) shows the decay of peak mean defect U_d^{peak} as a function of x/D for all four cases. The magnitude of U_d^{peak} for strongly stratified wakes ($Fr = 1.9$ and 1) is significantly higher than in the $Fr = \infty$ and 6 wakes, verifying that the longstanding hypothesis that stratified wakes 'live' longer (Spedding 1997). The U_d^{peak} values for $Fr = 1.9$ and $Fr = 1$ are 3–4 times higher than for $Fr = \infty$ and 6 by $x/D = 40$. We refrain from attempting to fit decay rates for the U_d^{peak} evolution since the streamwise domain available for curve fitting, approximately $30D$ from $x/D = 10$ onward, is relatively small for a high-confidence fit.

However, for the $Fr = 6$ wake, a careful reader can observe that the decay rate of U_d^{peak} slows down compared with the $Fr = \infty$ wake around $x/D \approx 20$ ($Nt \approx 3.33$). Ohh & Spedding (2024) also reported a similar slowdown in the decay of U_d for $Fr \geqslant 8$ wakes compared with the $Fr = \infty$ baseline around $Nt \approx 2$ (see their figure 17*b*).

In figure 12(*b*), the decay of area-integrated mean kinetic energy, $\{E_K^M\} = \int (U_d^2 + \langle u_y \rangle^2 + \langle u_z \rangle^2)/2 \, \mathrm{dA}$, is compared among the four cases. Circles of radii $r/D = 2$ and $r/D = 3.5$ are used as cross-sections for the stratified cases and the unstratified case, respectively, ensuring that the wakes remain inside the domain of integration for all x/D. The area-integrated energy in both $Fr = 1.9$ and 1 wakes is of comparable magnitude throughout the domain. Lee-waves-induced oscillations with wavelength approximately equal to $2\pi Fr$ are clearly visible in both $Fr = 1.9$ and $Fr = 1$ wakes. These lee-wave-induced oscillations were identified by Bonnier & Eiff (2002) as an 'accelerated' collapse in the U_d evolution profile. DNS simulations by Pal *et al.* (2017) showed that this 'accelerated' collapse region in the U_d profiles is actually an imprint of the surrounding steady lee waves, having (*a*) a time scale of $Nt = 2\pi$ and (*b*) a wavelength of $\lambda/D = 2\pi Fr$. This effect is particularly pronounced at $Fr \sim O(1)$, where the lee waves are the strongest. Ortiz-Tarin *et al.* (2019, 2023) observed similar lee-wave-induced modulations in the wake of 4:1 and 6:1 spheroids at zero-degree pitch angles. More recently, Ohh & Spedding (2024) reported the presence of these lee-wave-induced oscillations in the wake trajectory of non-zero pitch angle spheroids at $Fr \geqslant 8$ (see figures 13 and 14 in their manuscript), a phenomenon also present in figure 13.

The decay of the unstratified wake and the $Fr = 6$ wake $\{E_K^M\}$ remain similar until $x/D \approx 4$, after which the decay rate of the $Fr = 6$ wake increases compared with the unstratified wake until $x/D \approx 25$. At $x/D \approx 25$, the decay rate of $\{E_K^M\}$ reduces, implying that ultimately, the $Fr = 6$ wake will be more 'long-lived' than the $Fr = \infty$ wake, in agreement with previous experimental and numerical studies on stratified wakes.

5.3. *Evolution of wake geometry*

Figure 11 makes it clear that the wake of a prolate spheroid at a pitch angle exhibits a pronounced buoyancy effect both in terms of its centre and its length scales. Figure 13 presents the evolution of the wake centre and length scales in the spanwise and vertical direction as a function of x/D.

These quantities are calculated as follows:

$$\langle y^c \rangle = \frac{\int y U_d^2 \mathrm{dA}}{\int U_d^2 \mathrm{dA}}, \qquad \langle z^c \rangle = \frac{\int z U_d^2 \mathrm{dA}}{\int U_d^2 \mathrm{dA}}, \tag{5.1}$$

$$L_y^2 = \frac{\int (y - \langle y^c \rangle)^2 U_d^2 \mathrm{dA}}{\int U_d^2 \mathrm{dA}}, \qquad L_z^2 = \frac{\int (z - \langle z^c \rangle)^2 U_d^2 \mathrm{dA}}{\int U_d^2 \mathrm{dA}}, \tag{5.2}$$

where $\langle y^c \rangle$, $\langle z^c \rangle$ are the temporally averaged wake-centre coordinates and L_y, L_z are the mean wake length scales in the cross-sectional planes normal to the streamwise coordinate x.

Figure 13(*a*,*b*) presents the streamwise evolution of the wake centre in both the spanwise (y) and vertical (z) directions as a function of x/D. The four wakes under consideration exhibit distinct evolutions. The unstratified wake moves away from the centreline ($r/D = 0$ axis) as the flow evolves, with more pronounced movement in the vertical (z) direction compared with the spanwise (y) direction. Its drift in the z direction is associated with the induced downward velocity at the centre of the counter-rotating streamwise vortex pair in

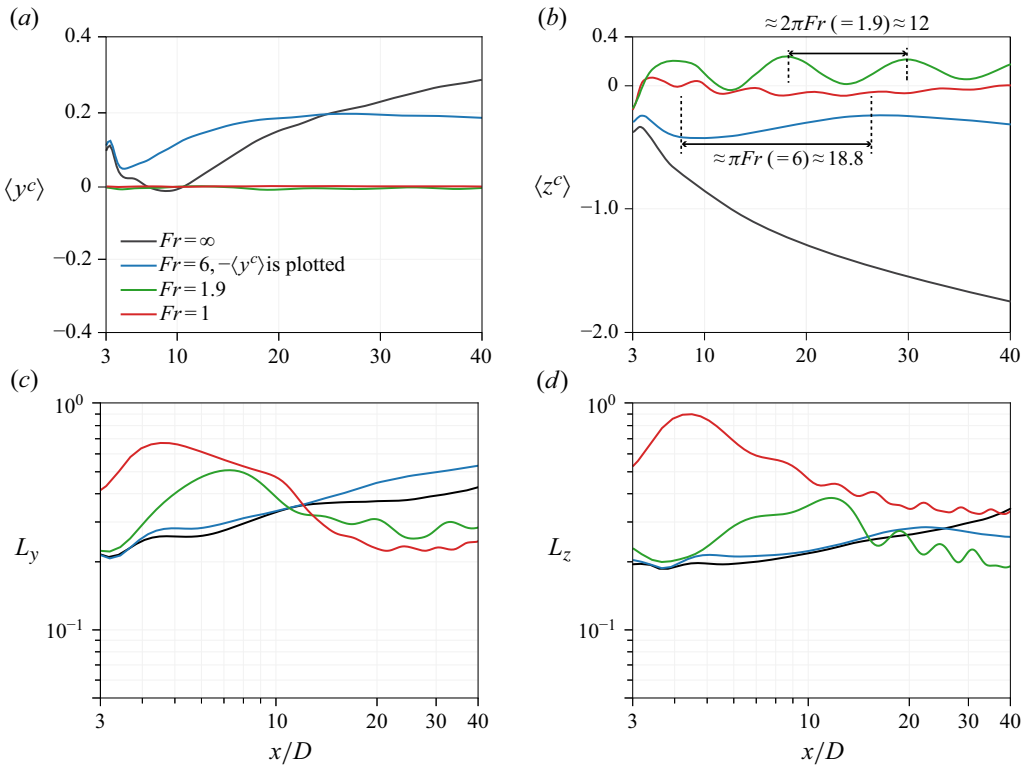

Figure 13. Evolution of wake centre in the (*a*) horizontal ($\langle y^c \rangle$) and (*b*) vertical ($\langle z^c \rangle$) directions. Evolution of wake (*c*) horizontal (L_y) and (*d*) vertical (L_z) length scales. In panel (*a*), $-\langle y^c \rangle$ is plotted for $Fr = 6$ to compare the magnitudes of lateral displacement of wake of $Fr = \infty$ and 6 wakes.

the separated flow, as will be discussed in § 6. The drift in the y direction is due to the initial lateral asymmetry of the wake vortices with one vortex being larger than the other.

Despite its relatively weak stratification, the descent of the $Fr = 6$ wake is strongly modified by buoyancy as seen in the trajectory of $\langle z^c \rangle$. The descent rate is already smaller than its unstratified counterpart at $x/D = 4$, a mere body diameter behind the trailing edge of the spheroid. At $x/D \approx 10$, the wake descent changes to an ascent until the wake reaches its neutral configuration. The locations of maximum descent and ascent of the wake are separated by $\pi Fr \approx 18.8$, demonstrating that even at a relatively weaker stratification of $Fr = 6$, the wake is strongly influenced by the surrounding lee waves. The lee-wave-induced modulation of the wake trajectory in the vertical direction aligns with the findings of Ohh & Spedding (2024), who reported a similar modulation with a wavelength of $\lambda/D = 2\pi Fr$ for their $Re_L = 30\,000$, $Fr = 8$ and $\alpha = 20°$ wake (see their figure 8*d*). To compare the lateral drift magnitude with that of the unstratified wake, we plot $-\langle y^c \rangle$ in figure 13(*a*) for the $Fr = 6$ wake. While the lateral drift is comparable in magnitude near the body, the two cases diverge significantly beyond $x/D \approx 5$, highlighting notable qualitative and quantitative differences in the wake trajectory evolution between the $Fr = \infty$ and 6 wakes.

The values of $\langle y^c \rangle$ of the $Fr = 1.9$ and $Fr = 1$ wakes remain zero throughout their evolution (figure 13*a*). In the vertical direction, the $Fr = 1.9$ wake shows a lee-waves-induced oscillation in the $\langle z^c \rangle$ trend (figure 13*b*), also evident in contours of U_d of the $Fr = 1.9$ wake (figure 11*c*,*g*,*k*,*o*). Interestingly, $\langle z^c \rangle$ of the $Fr = 1$ wake also stays close

to zero, which implies that the U_d^2 weighted mean of the vertical coordinate of the two distinct lobes of the double wake in figure 11(*d*,*h*,*l*,*p*) approximately balance each other out. Both $Fr = 1$ and 1.9 wakes show a clear lee-waves-induced oscillation in the $\langle z^c \rangle$ evolution with wavelength equal to $2\pi Fr$.

5.4. *Evolution of wake length scales*

Figures 13(*c*) and 13(*d*) show the evolution of horizontal (L_y) and vertical (L_z) length scales, respectively. Here, L_y and L_z of the $Fr = \infty$ and 6 wakes evolve similarly in rate and magnitude until $x/D \approx 15$ ($Nt \approx 2.5$). Beyond $x/D \approx 25$ ($Nt \approx 4$), the growth of L_z in the $Fr = 6$ wake slows down owing to the increasing influence of stratification. The Nt location of this reduction in the growth rate of L_z is consistent with the findings of Ohh & Spedding (2024), who reported that the L_z of their stratified wakes deviated from that of the unstratified wake at $Nt \sim 2{-}4$ for $\alpha = 20°$ and $Fr \geqslant 8$ (see their figure 17). Furthermore, to preserve momentum deficit, i.e. $U_d L_y L_z \sim$ constant, L_y increases for the $Fr = 6$ wake as compared with the $Fr = \infty$ wake (see figure 13*c*). The streamwise location of the reduction in the growth rate of L_z for the $Fr = 6$ wake aligns with the decrease in the decay rates of U_d and E_K^M (figure 12). This contraction of L_z (compared with the $Fr = \infty$ wake) in conjunction with the decreased decay of U_d has been widely reported in stratified wake literature of spheroids (Ortiz-Tarin *et al.* 2019, 2023) as well as other bluff bodies (Chongsiripinyo & Sarkar 2020; Pal *et al.* 2017) for a variety of Re and Fr values. The contours of wake defect velocity (figure 11) revealed the strong coupling of the wake topology to the isopycnal geometry, which in turn is significantly modified by the steady lee wave field (Bonnier & Eiff 2002; Pal *et al.* 2017) at $Fr = 1.9$ and 1. The behaviour of L_y and L_z reflects this coupling. Additionally, the buoyancy effect on flow separation in the cases with higher relative stratification is also important. For example, L_z at $Fr = 1$ is significantly larger than in the other cases until almost the end of the domain owing to the structure of the $Fr = 1$ wake (figure 11*d*,*h*,*l*,*p*) with an upper and a lower lobe. Owing to the peculiar geometry of the $Fr = 1$ wake, calculation of L_z using (5.2) underestimates its vertical extent. Visually, the $Fr = 1$ wake is discernible within $z = \pm 0.7$ in figure 11(*d*,*h*,*l*,*p*).

6. Evolution of mean streamwise vorticity

Shifting focus from the mean wake evolution, we now delve into the dynamics of streamwise vortices that develop at the body and into the wake. Figure 14 presents the distribution of instantaneous streamwise vorticity ω_x at positions $x/D = 0$, 1, 2 and 2.75 on the body. Views at these four locations from both the left and right perspectives are provided to provide a complete picture. The flow remains laminar over the body for all Fr values at the present $Re_L = 30\,000$ until it separates.

At both $Fr = \infty$ and $Fr = 6$, the counter-rotating vortex pair is evident as early as the body centre ($x/D = 0$), see figure 14(*a*–*d*). The development is similar on both sides until $x/D = 1$, maintaining symmetry about the vertical centreplane of the spheroid. However, at $x/D = 2$, lateral asymmetry emerges as one side undergoes a stronger vortex rollup than the other. As was surmised from the U_d contours, the polarity of the stronger vortex is reversed at $Fr = 6$ relative to $Fr = \infty$. Specifically, the positive vortex filament (figure 14*b*) is larger at $Fr = \infty$ in contrast to $Fr = 6$ (figure 14*c*) where the negative vortex filament is larger. At $x/D = 2.75$, the vortex asymmetry becomes even more pronounced in both cases, consistent with the asymmetry in U_d (figure 11) and force coefficients (figure 10). Previous studies on slender bodies have documented the presence of asymmetry in a counter-rotating vortex pair under two conditions: (*a*) at high pitch angle α and moderate

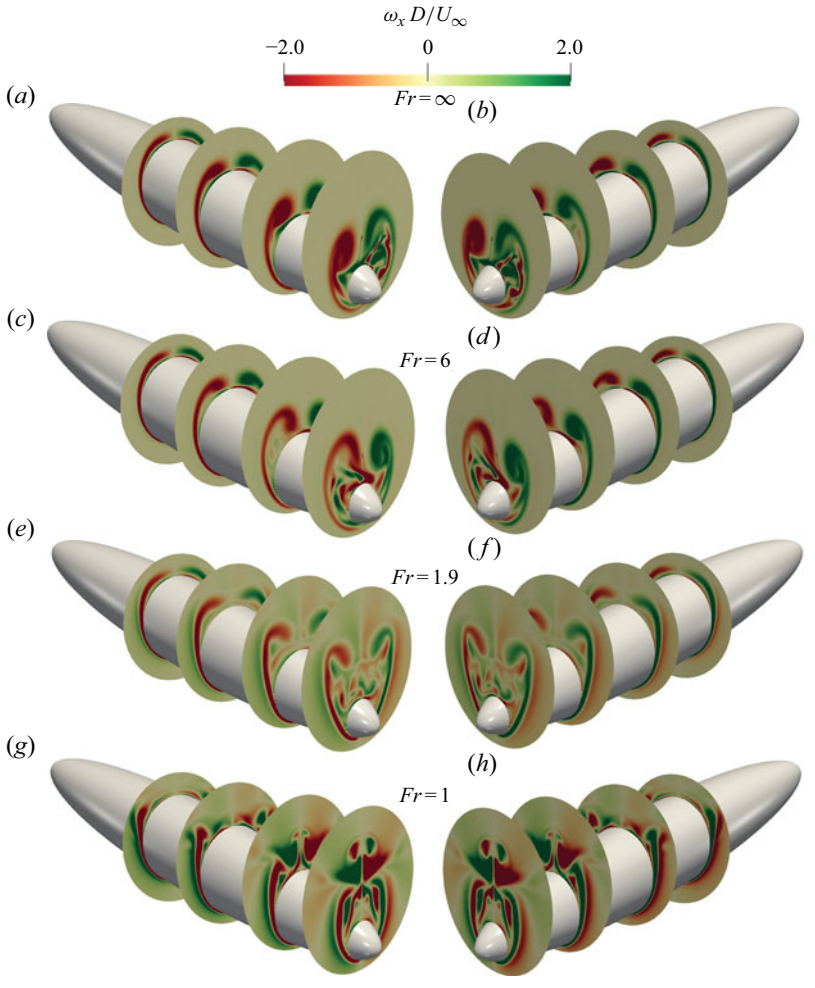

Figure 14. Instantaneous streamwise vorticity (ω_x) on the spheroid at $x/D = 0$, 1, 2 and 2.75 for all Fr at $\alpha = 10°$. Views from the (a,c,e,g) left and (b,d,f,h) right.

Reynolds numbers Re (Jiang *et al.* 2014, 2015, 2016); or (b) at moderate α and high Re (Ashok *et al.* 2015*a*). The present study reports lateral vortex asymmetry in yet another unstratified wake, namely moderate α and moderate Re. Furthermore, the study reveals that this asymmetry persists for mild stratifications too, until Fr decrease to 6.

Vortex asymmetry is absent at the stronger relative stratifications of $Fr = 1.9$ and 1. Additionally, the vortex-pair geometry changes. For example, the two filaments at $x/D = 2.75$ in the $Fr = 1.9$ wake appear thinner and less curved than at $Fr = \infty$ or 6. At $Fr = 1$, the vorticity field becomes even more complex. There is a primary vortex pair whose filaments roll up even less than that at $Fr = 1.9$. Furthermore, the region above the vortex pair also contains ω_x, unlike the other three cases (compare the $x/D = 2.75$ slice between the bottom row and other three rows). This distinct upper region of ω_x corresponds to the upper lobe of the double-lobed mean wake structure in figure 11(d).

6.1. *Streamwise vortex pair in the unstratified wake*

The downstream evolution of the counter-rotating vortex pair is of interest. Figure 15 presents $\langle\omega_x\rangle$ contours at four locations in the wake, $x/D = 3$, 10, 20 and 30. The black

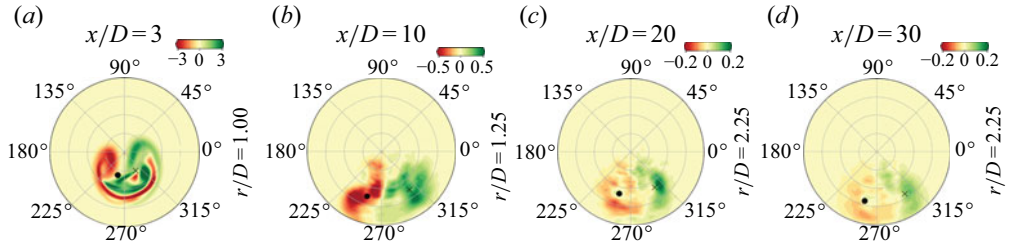

Figure 15. Mean streamwise vorticity $\langle\omega_x\rangle$ contours at $x/D = 3$, 10, 20 and 30 for $Fr = \infty$. r/D denotes the radial extent of the contour at the respective x/D locations. The black dot and cross represent the centre of the negative and the positive vortex filament, respectively.

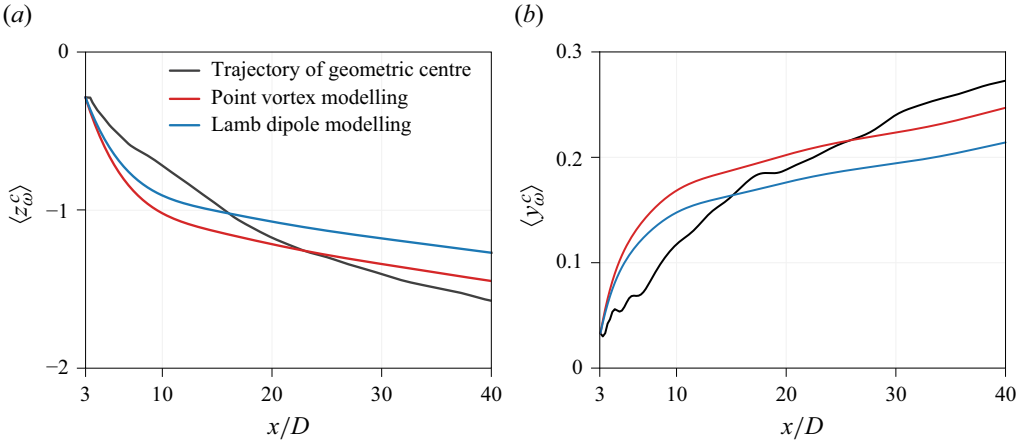

Figure 16. Location of the streamwise vortex pair in the $y-z$ plane as a function of x/D. $\langle z_\omega^c\rangle$ and $\langle y_\omega^c\rangle$ denote the evolution in the vertical and spanwise direction, respectively. Results from the point and Lamb dipole modelling are shown for the geometrical centre of the centroids of the negative and positive vortex.

circle and cross show the centroid of the positive and negative vortex filaments, which are computed following Jemison *et al.* (2020):

$$\langle y_\omega^{c(+,-)}\rangle = \frac{\int y\langle\omega_x\rangle^{(+,-)}\mathrm{dA}}{\int\langle\omega_x\rangle^{(+,-)}\mathrm{dA}}, \qquad \langle z_\omega^{c(+,-)}\rangle = \frac{\int z\langle\omega_x\rangle^{(+,-)}\mathrm{dA}}{\int\langle\omega_x\rangle^{(+,-)}\mathrm{dA}}, \tag{6.1}$$

where $+$ and $-$ denote the positive and the negative vortex filament, respectively.

The asymmetric vortex pair on the body propagates downstream as two distinct patches of $\langle\omega_x\rangle$. The centroids exhibit downward descent as well as lateral shifts. It is worth noting that, despite the spatial asymmetry in the organisation of the negative and positive filaments, the magnitudes of their time-averaged circulation remain equal throughout the computational domain, i.e. $\langle\Gamma^+\rangle = -\langle\Gamma^-\rangle$, owing to the conservation of angular momentum.

Figure 16 provides a comparison of the actual trajectoriy of the geometric centre of the two vortices with the predictions of point vortex and Lamb dipole models. In an unstratified medium, according to the point vortex approximation, the vortex pair travels in its plane with the following vortex-induced velocity (Hill 1975):

$$\boldsymbol{V}(x) = \frac{\langle\Gamma\rangle(x)}{2\pi d}\boldsymbol{n}. \tag{6.2}$$

Here, $\langle\Gamma\rangle(x)$ represents the time-averaged circulation in constant-x planes, $\boldsymbol{n}$ is the unit normal to the vector $\boldsymbol{d}$ between the positive and negative vortex centroids, and d is the

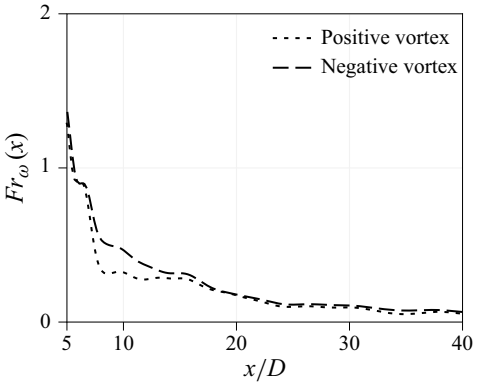

Figure 17. Variation of Fr_ω, the hypothetical Froude number of the counter-rotating streamwise vortex pair in the $Fr=\infty$ wake if subjected to $Fr=6$ stratification, as a function of streamwise distance x for both positive and negative vortex filaments.

magnitude of $\boldsymbol{d}$. Assume that the vortex pair moves with constant speed U_∞ in the x direction so that the vortex travel time is $t=x/U_\infty$ and integrate $\boldsymbol{V}(t=x/U_\infty)$ with respect to t. The result is the vortex centroid displacement in y- and z-directions under the point vortex modelling assumption. The Lamb dipole modelling follows the same approach, e.g. Flór *et al.* (1994):

$$\boldsymbol{V}=\frac{\langle\Gamma\rangle}{(6.83^2/2\pi)d}\boldsymbol{n}\,. \tag{6.3}$$

Both the point vortex and Lamb dipole models overestimate the vertical displacement magnitude (figure 16*a*) until $x/D\approx 15-20$ followed by an overestimate. These models satisfactorily capture the spanwise drift of the geometric centre of the vortex pair (figure 16*b*). While the simplified models capture the order of magnitude of the vertical and horizontal vortex displacement in the current unstratified simulation until $x/D=40$, the accuracy of these simplified models is marginal in capturing the streamwise trend, indicating that the spatial organisation of the vortices shed from the body is more complex than that of a point-vortex pair.

6.2. *Buoyancy effects on the streamwise vorticity*

The $Fr=6$ wake showed a significant reduction in the wake descent ($\langle z^c\rangle$ in figure 13(*b*) as early as $x/D=4$, only 1 body diameter behind the trailing edge of the spheroid, or at $Nt=2/3$ in buoyancy units behind the body centre. This relatively early buoyancy effect, despite a relatively weak initial stratification of $Fr=6$, can be understood by consideration of the hypothetical Froude number ($Fr_\omega(x)$) if the vortex pair in the unstratified wake was subjected to the buoyancy frequency (N) of the $Fr=6$ case. Here, $Fr_\omega(x)=W_c(x)/Nd(x)$, where $W_c(x)=\mathrm{d}\langle z^c_\omega\rangle/\mathrm{d}t=U_\infty\mathrm{d}\langle z^c_\omega\rangle/\mathrm{d}x$ is the measured descent velocity, and $d(x)$ is the distance between the centroids of the positive and negative vortex. Remarkably, Fr_ω is already $O(1)$ by $x/D\approx 5$ (figure 17), indicating that the streamwise vortices of the $Fr=\infty$ cases would be strongly impacted by buoyancy, right from the beginning, if exposed to the $Fr=6$ stratification. In what follows, we will delve deeper into the effect of buoyancy on streamwise wake vortices.

Figure 18 displays the contours of $\langle\omega_x\rangle$ for the stratified wakes. At $x/D=3$, the presence of counter-rotating streamwise vorticity is evident across all three stratified cases. Buoyancy significantly affects the subsequent streamwise variation of $\langle\omega_x\rangle$. With

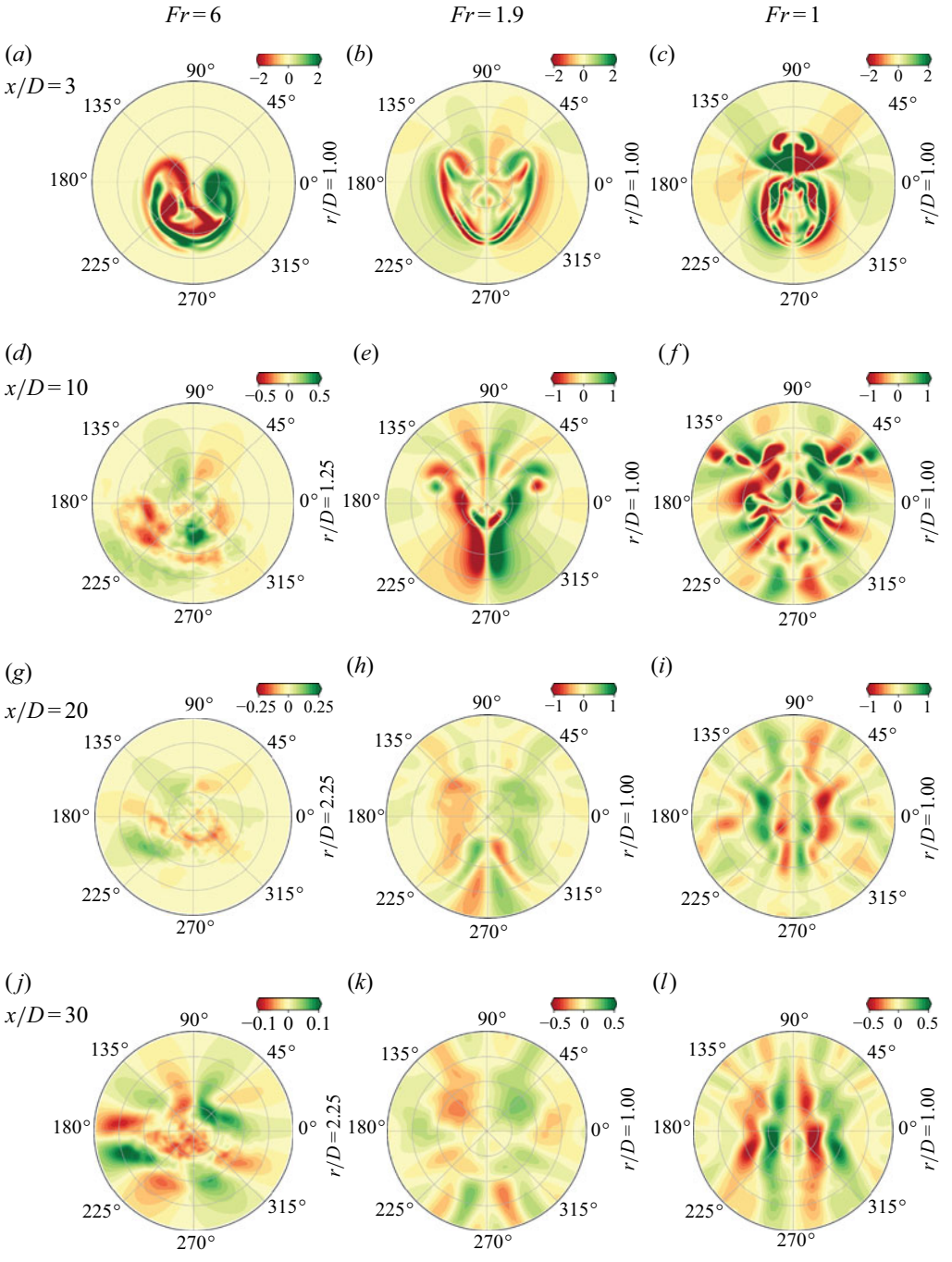

Figure 18. Mean streamwise vorticity $\langle\omega_x\rangle$ at $x/D = 3$, 10, 20, 30 for $Fr = 6$, 1.9 and 1. r/D denotes the radial extent of the contour at the respective x/D locations.

decreasing Fr, not only does the magnitude of $\langle\omega_x\rangle$ increase, but also its spatial organisation.

Notably, in the $Fr = 6$ wake (figure 18*a,d,g,j*), the integrity of the streamwise counter-rotating vortex filaments disintegrates rapidly, unlike the $Fr = \infty$ wake. This buoyancy

effect will be attributed to the baroclinic torque shortly. Given the absence of distinct positive and negative vortex filaments in the $Fr = 6$ wake, a simplified point vortex or Lamb vortex model prediction is not attempted. In the case of stronger relative stratifications of $Fr = 1.9$ and 1, the $\langle\omega_x\rangle$ fields exhibit increased complexity at $x/D = 10$ and beyond. These wakes display a larger spatial extent of $\langle\omega_x\rangle$ owing to steady lee waves outside the wake core. Also, the interaction between the wake vorticity and the lee waves vorticity is intricate, making it challenging to discern the fate of the shed vortices based solely on the contours, in contrast to the $Fr = \infty$ wake.

The baroclinic torque, which measures the direct influence of buoyancy on vorticity, is useful to understand the observed dependence of $\langle\omega_x\rangle$ on Fr. On taking the curl of the Reynolds average of (2.2), it follows that there is a baroclinc torque

$$\begin{aligned} \boldsymbol{\omega}_{BT} &= -\frac{1}{Fr^2}\boldsymbol{\nabla}\times\langle\rho_d\rangle\boldsymbol{e}_3 \\ (\omega_{BT})_i &= -\frac{1}{Fr^2}\epsilon_{ijk}\frac{\partial\langle\rho_d\rangle}{\partial x_j}\delta_{k3} = -\frac{1}{Fr^2}\epsilon_{ij3}\frac{\partial\langle\rho_d\rangle}{\partial x_j}. \end{aligned} \tag{6.4}$$

The mean streamwise contribution of the baroclinic torque is $\omega_{BTx} = -(1/Fr)^2\partial\langle\rho\rangle/\partial y$ and follows from (6.4) with $i = 1$. It involves only the lateral (spanwise) mean buoyancy gradient, apart from the Fr-dependent normalisation factor.

The magnitude of ω_{BTx} is substantial and increases with increasing stratification (figure 19). At $x/D = 3$, it is especially large at the wake boundaries as suggested by the organisation of mean isopycnals in figure 11. Further downstream, the contribution of lee waves to ω_{BTx} becomes progressively important. For $Fr = 6$, the initial distribution of $-(1/Fr)^2\partial\langle\rho\rangle/\partial y$ (figure 19*a*) is laterally asymmetric since transport by the laterally asymmetric flow in the $Fr = 6$ wake (evident through the previous analyses) leads to buoyancy asymmetry. In contrast, the $Fr = 1.9$ and 1 cases exhibit lateral symmetry except for a sign change upon spanwise reflection. This contrast is evident when comparing the left column to the right two columns in figure 19. As these wakes progress downstream, the coherence of the baroclinic torque field in the $Fr = 6$ wake diminishes significantly when compared with the $Fr = 1$ and 1.9 wakes.

7. Summary and conclusions

The stratified wake of a 6:1 prolate spheroid at angle of attack $\alpha = 10°$ is studied using large eddy simulations (LES). Cases with $Fr = U_\infty/ND = 6$, 1.9 and 1 are simulated along with its unstratified ($Fr = \infty$) counterpart at a length-based Reynolds number $Re_L = U_\infty L/\nu = 30\,000$. The focus of the present manuscript is on the mean wake and vorticity dynamics along with the on-body flow. Subsequent work that includes higher values of Re_L will report on turbulence, unsteady coherent structures and mixing aspects.

Visualisations of instantaneous u_x-isovolumes, streamlines and λ_2-structures (figures 4–7) reveal overall changes in flow topology as Fr decreases. At $Fr = \infty$ and $Fr = 6$, flow separation at the body aligns with previous findings in the literature. In both cases, a pair of streamwise vortices emerges from the lateral sides of the body, initially laminar, but transitioning to turbulence near the spheroid. Even at the relatively weaker stratification of $Fr = 6$, stratification effects are evident. Similar to the observations by Ohh & Spedding (2024), the wake at $Fr = 6$ does not descend as much as the $Fr = \infty$ wake, due to buoyancy forces inhibiting vertical displacement. As stratification strength increases, the wake topology and streamline distribution change significantly. Small-scale variability (turbulence) in the wake is inhibited at $Fr = 1.9$ and

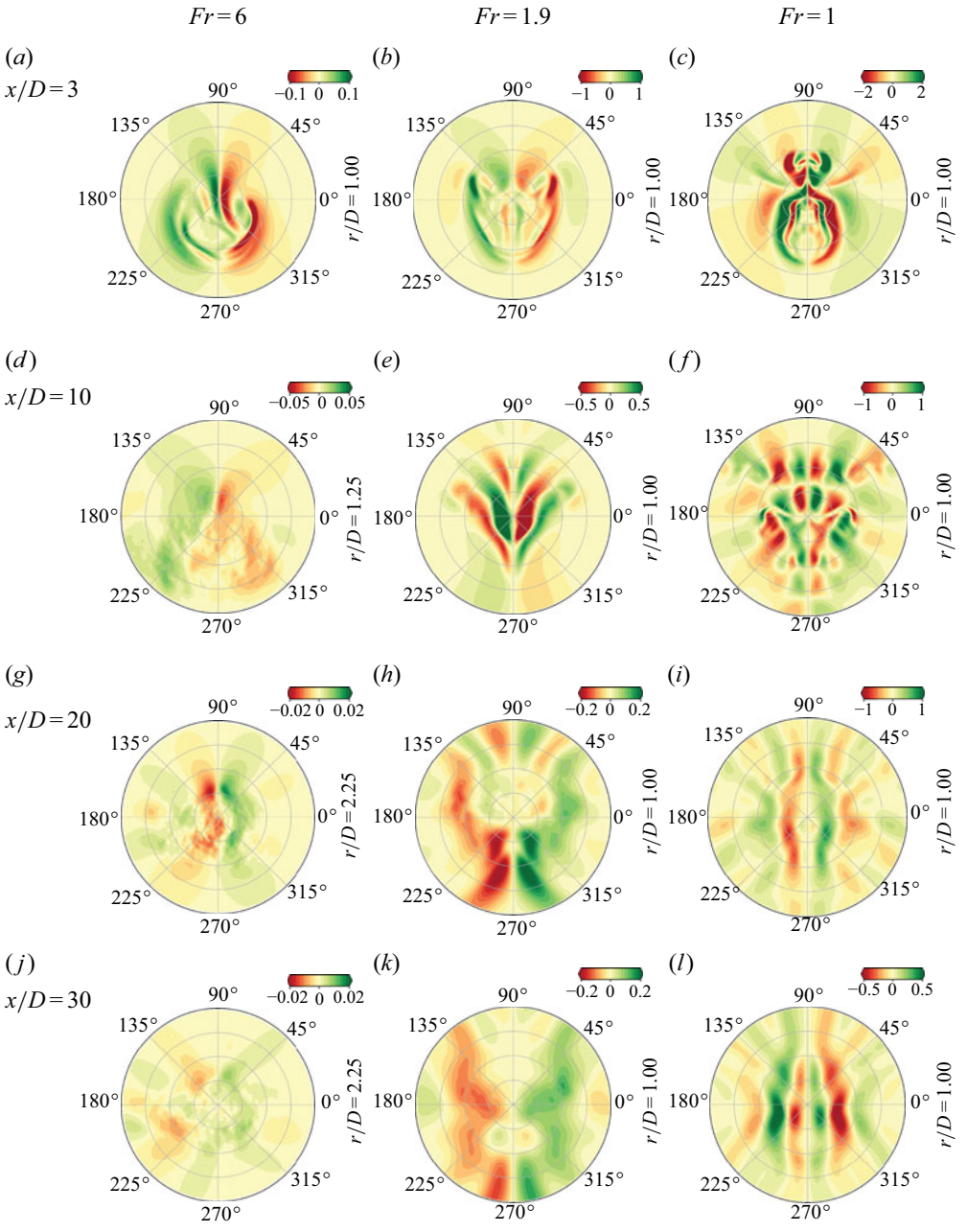

Figure 19. Mean streamwise baroclinic torque $-1/Fr^2 \partial\langle\rho\rangle/\partial y$ at $x/D = 3$, 10, 20, 30 for $Fr = 6$, 1.9 and 1. r/D denotes the radial extent of the contour at the respective x/D locations. Note that as x/D increases, colourbar limits are reduced to accentuate the spatial structure of the mean streamwise baroclinic torque.

$Fr = 1$. At $Fr = 1.9$, the λ_2-structures and u_x-isovolumes remain laminar up to $x/D = 20$, with even later transition at $Fr = 1$.

The analysis of averaged pressure and friction contours on the spheroid provides further insight into the effect of stratification on the mean flow at the spheroid. Specifically, the C_f contours across different Fr values reveal that stratification alters the flow separation

topology (figure 9). At $Fr = \infty$ and $Fr = 6$, flow separates from both sides of the body. However, at $Fr = 1.9$, flow separation occurs from both sides as well as the central region ($y/D = 0$). By $Fr = 1$, lateral separation is completely suppressed since the cross-stream windward-to-leeward surface flow is arrested by buoyancy. Furthermore, $Fr = \infty$ and 6 exhibit asymmetric separation, quantified further by C_y in both cases (figure 10). At stronger stratifications, the overturning motion in the vortex rollup weakens as evidenced by the secondary flow streamlines (figure 6) and the vorticity is no longer laterally asymmetric.

The evolution of the mean wake topology, both quantiatively and qualitatively, is also analysed for all four Fr cases. In unstratified conditions and in the $Fr = 6$ case, the initial wake drifts both in the vertical and horizontal direction owing to vertical momentum imparted by non-zero α and initial lateral asymmetry present in the flow (figure 11*a*,*e*,*i*,*m*). Previous studies on flow past slender bodies at both high (Jiang *et al.* 2014, 2015, 2016) and low-to-moderate (Ashok *et al.* 2015*a*,*b*) angles of attack have found lateral asymmetry in the wake. We hypothesise that the $Fr = \infty$ (and $Fr = 6$) flows at $Re_L = 30\,000$ are bistable, being locked in two distinct reflectional-symmetry-breaking states, with each state being equally probable. The above-mentioned studies reporting flow asymmetry also found that the orientation of asymmetry remained constant over time, similar to our findings for both $Fr = \infty$ and $Fr = 6$. A caveat is that the present averaging time span of approximately $100D/U_\infty$ is not long and the polarity could conceivably switch at longer times, although it did not do so in the laboratory experiments of Ashok *et al.* (2015*a*,*b*).

Interestingly, the effect of stratification on the wake is evident in the $Fr = 6$ wake from the outset. Specifically, focusing on the vertical motion (a descent in the present configuration) of the wake centre $\langle z^c \rangle$ (figure 13) owing to the self-induced velocity of the vortex pair, it is found that the descent of the $Fr = 6$ wake is inhibited from approximately $x/D \approx 3$. A Froude number (Fr_ω) based on the baseline unstratified descent velocity and N is found to become $O(1)$ in the near wake, explaining the rapid arrest of the wake descent by buoyant deceleration. Subsequent oscillation in the evolution of $\langle z^c \rangle$ with a wavelength $\lambda = 2\pi Fr$, consistent with observations by Ohh & Spedding (2024), is also observed. As Fr is reduced further, the mean wake topology becomes more influenced by stratification. At $Fr = 1.9$, the vertical wake drift decreases further and the wake oscillates with a significantly stronger amplitude than at $Fr = 6$. The $Fr = 1$ case exhibits a unique wake topology, featuring two distinct lobes due to the different separation patterns, which persist until at least $x/D = 40$. Higher Re_L studies at $Fr = 1$ in this configuration are necessary to assess whether turbulent mixing at high Re_L would prevent formation and persistence of the intriguing double-lobed wake found here.

The streamwise evolution trends of key mean wake quantities like U_d, mean kinetic energy and wake length scales (L_y and L_z) are qualitatively similar to previous studies of stratified wakes (Spedding 1997; Bonnier & Eiff 2002; Pal *et al.* 2017; Ortiz-Tarin *et al.* 2019): (*a*) lee-waves-induced modulation is observed in all stratified wakes, with its intensity increasing with decreasing Fr; (*b*) $Fr = 1.9$ and 1 wakes retain significantly higher MKE and U_d than $Fr = 6$ or the unstratified wake; and (c) the deviation in area-integrated quantities in the $Fr = 6$ wake from the $Fr = \infty$ wake occurs at $Nt \sim 1{-}3$.

Shifting the focus to the mean vorticity dynamics in the wake, it was found that the asymmetry in the $Fr = \infty$ and 6 wakes originates from the earlier roll-up of the vortex on one side compared with the other (see figure 14*a*–*d*). At $Fr = 1.9$ and 1, the roll-up is significantly inhibited by buoyancy (see figure 14*e*–*h*), leading to a symmetric configuration of the streamwise vortex pair. The negative and positive vortices maintain a clear signature for $Fr = \infty$ (figure 15), prompting an attempt to model them using point vortex and Lamb dipole approaches to capture the trends in vertical descent and

spanwise displacement of the vortex pair. While these rudimentary models provide an order of magnitude estimate for the vertical descent and spanwise displacement (figure 16), they do not accurately capture the streamwise trend since the topology of the relatively close spheroid vortices is more complex than a pair of pointwise vortices. At $Fr = 6$, the streamwise vortex pair loses coherence as early as $x/D = 10$ (figure 18*d*), preventing any attempts at similar modelling for the $Fr = 6$ wake. The $Fr = 1.9$ and 1 wakes exhibit a significantly more complex spatial distribution due to nonlinear interactions between the vorticity carried by the wake and that carried by the steady lee waves. The influence of steady lee waves is evident in both $\langle \omega_x \rangle$ and baroclinic torque contours for $Fr = 1.9$ and 1 (figure 18 and 19).

The findings of this work suggest that energetic, weakly stratified wakes at $Fr \sim O(10)$ need to be investigated at a higher Re_L to confirm whether, close to the body, there is strong buoyancy-induced modification of the wake descent and structure at these elevated Reynolds numbers, similar to what is observed in the $Fr = 6$ wake of this study. Future simulations of $Fr \sim O(1)$ wakes will help better understand how the transition to turbulence might occur at higher Re_L and how wake mixing takes place, an aspect that is strongly suppressed in the $Fr = 1$ case of this study. Finally, larger values of pitch angle are also deserving of study.

Funding. We gratefully acknowledge the support of ONR grant N00014-20-1-2253. Computational resources were provided by the Department of Defense High Performance Computing Modernization Program.

Declaration of interests. The authors report no conflict of interest.

Author contributions. S.N. and S.J. contributed equally to this work.

References

Ashok, A., Van Buren, T. & Smits, A.J. 2015*a* Asymmetries in the wake of a submarine model in pitch. *J. Fluid Mech.* **774**, 416–442.

Ashok, A., Van Buren, T. & Smits, A.J. 2015*b* The structure of the wake generated by a submarine model in yaw. *Exp Fluids* **56** (6), 123.

Balaras, E. 2004 Modeling complex boundaries using an external force field on fixed Cartesian grids in large-eddy simulations. *Comput. Fluids* **33** (3), 375–404.

Bonnier, M. & Eiff, O. 2002 Experimental investigation of the collapse of a turbulent wake in a stably stratified fluid. *Phys. Fluids* **14** (2), 791–801.

Bridges, D. 2006 The Asymmetric Vortex Wake Problem - Asking the Right Question. In *36th AIAA Fluid Dynamics Conference and Exhibit*. American Institute of Aeronautics and Astronautics.

Brucker, K.A. & Sarkar, S. 2010 A comparative study of self-propelled and towed wakes in a stratified fluid. *J. Fluid Mech.* **652**, 373–404.

Chevray, R. 1968 The turbulent wake of a body of revolution. *ASME J. Basic Engng* **90** (2), 275–284.

Chongsiripinyo, K. & Sarkar, S. 2020 Decay of turbulent wakes behind a disk in homogeneous and stratified fluids. *J. Fluid Mech.* **885**, A31.

Constantinescu, G.S., Pasinato, H., Wang, Y., Forsythe, J.R. & Squires, K.D. 2002 Numerical investigation of flow past a prolate spheroid. *J. Fluids Engng* **124** (4), 904–910.

Dairay, T., Obligado, M. & Vassilicos, J.C. 2015 Non-equilibrium scaling laws in axisymmetric turbulent wakes. *J. Fluid Mech.* **781**, 166–195.

Dommermuth, D.G., Rottman, J.W., Innis, G.E. & Novikov, E.A. 2002 Numerical simulation of the wake of a towed sphere in a weakly stratified fluid. *J. Fluid Mech.* **473**, 83–101.

Flór, J.B., Van, H. & Gertijan, J.F. 1994 An experimental study of dipolar vortex structures in a stratified fluid. *J. Fluid Mech.* **279**, 101–133.

Fu, T.C., Shekarriz, A., Katz, J. & Huang, T.T. 1994 The flow structure in the lee of an inclined 6: 1 prolate spheroid. *J. Fluid Mech.* **269**, 79–106.

Germano, M., Piomelli, U., Moin, P. & Cabot, W.H. 1991 A dynamic subgrid-scale eddy viscosity model. *Phys. Fluids* **3** (7), 1760–1765.

Grandemange, M., Gohlke, M. & Cadot, O. 2013 Turbulent wake past a three-dimensional blunt body. Part 1. Global modes and bi-stability. *J. Fluid Mech.* **722**, 51–84.

HAN, T. & PATEL, V.C. 1979 Flow separation on a spheroid at incidence. *J. Fluid Mech.* **92** (4), 643–657.
HILL, F.M. 1975 A numerical study of the descent of a vortex pair in a stably stratified atmosphere. *J. Fluid Mech.* **71** (1), 1–13.
JEMISON, M.B., DELANEY, K. & KANNEPALLI, C. 2020 A study on the effect of an experimental sting on the wake of a prolate spheroid. In *AIAA Scitech 2020 Forum*, pp. 1755.
JIANG, F., ANDERSSON, H.I., GALLARDO, J.P. & OKULOV, V.L. 2016 On the peculiar structure of a helical wake vortex behind an inclined prolate spheroid. *J. Fluid Mech.* **801**, 1–12.
JIANG, F., GALLARDO, J.P. & ANDERSSON, H.I. 2014 The laminar wake behind a 6: 1 prolate spheroid at 45° incidence angle. *Phys. Fluids* **26** (11), 113602.
JIANG, F., GALLARDO, J.P., ANDERSSON, H.I. & ZHANG, Z. 2015 The transitional wake behind an inclined prolate spheroid. *Phys. Fluids* **27** (9), 093602.
JIMENEZ, J.M., HULTMARK, M. & SMITS, A.J. 2010 The intermediate wake of a body of revolution at high Reynolds numbers. *J. Fluid Mech.* **659**, 516–539.
KUMAR, P. & MAHESH, K. 2018 Large-eddy simulation of flow over an axisymmetric body of revolution. *J. Fluid Mech.* **853**, 537–563.
LI, J.J.L., YANG, X.I.A. & KUNZ, R.F. 2024 Direct numerical simulation of temporally evolving stratified wakes with ensemble average. *J. Fluid Mech.* **980**, A3.
LIN, Q., LINDBERG, W.R., BOYER, D.L. & FERNANDO, H.J.S. 1992 Stratified flow past a sphere. *J. Fluid Mech.* **240**, 315–354.
MADISON, T.J., XIANG, X. & SPEDDING, G.R. 2022 Laboratory and numerical experiments on the near wake of a sphere in a stably stratified ambient. *J. Fluid Mech.* **933**, A12.
MEUNIER, P. & SPEDDING, G.R. 2006 Stratified propelled wakes. *J. Fluid Mech.* **552**, 229–256.
NEDIĆ, J., VASSILICOS, J.C. & GANAPATHISUBRAMANI, B. 2013 Axisymmetric turbulent wakes with new nonequilibrium similarity scalings. *Phys. Rev. Lett.* **111** (14), 1–5.
NELSON, R.C., CORKE, T.C. & MATSUNO, T. 2006 Visualization and control of fore-body vortices. In *Proceedings of the 12th ISFV*, pp. 1–11. Optimage Ltd. Edinburgh, UK.
NELSON, R.C. & PELLETIER, A. 2003 The unsteady aerodynamics of slender wings and aircraft undergoing large amplitude maneuvers. *Prog. Aerosp. Sci.* **39** (2-3), 185–248.
OHH, C. & SPEDDING, G.R. 2024 The effects of stratification on the near wake of 6 : 1 prolate spheroid. *J. Fluid Mech.* **997**, A43.
ORLANSKI, I. 1976 A simple boundary condition for unbounded hyperbolic flows. *J. Comput. Phys.* **21** (3), 251–269.
ORTIZ-TARIN, J.L., CHONGSIRIPINYO, K.C. & SARKAR, S. 2019 Stratified flow past a prolate spheroid. *Phys. Rev. Fluids* **4** (9), 094803.
ORTIZ-TARIN, J.L., NIDHAN, S. & SARKAR, S. 2021 High-Reynolds-number wake of a slender body. *J. Fluid Mech.* **918**, A30.
ORTIZ-TARIN, J.L., NIDHAN, S. & SARKAR, S. 2023 The high-Reynolds-number stratified wake of a slender body and its comparison with a bluff-body wake. *J. Fluid Mech.* **957**, A7.
PAL, A., SARKAR, S., POSA, A. & BALARAS, E. 2017 Direct numerical simulation of stratified flow past a sphere at a subcritical Reynolds number of 3700 and moderate Froude number. *J. Fluid Mech.* **826**, 5–31.
PATEL, V.C. & KIM, S.E. 1994 Topology of laminar flow on a spheroid at incidence. *Comp. Fluids* **23** (7), 939–953.
PIQUET, J. & QUEUTEY, P. 1992 Navier–Stokes computations past a prolate spheroid at incidence—I. Low incidence case. *Comp. Fluids* **21** (4), 599–625.
PLASSERAUD, M., KUMAR, P. & MAHESH, K. 2023 Large-eddy simulation of tripping effects on the flow over a 6 : 1 prolate spheroid at angle of attack. *J. Fluid Mech.* **960**, A3.
POSA, A. & BALARAS, E. 2016 A numerical investigation of the wake of an axisymmetric body with appendages. *J. Fluid Mech,.* **792**, 470–498.
RIGAS, G., OXLADE, A.R., MORGANS, A.S. & MORRISON, J.F. 2014 Low-dimensional dynamics of a turbulent axisymmetric wake. *J. Fluid Mech.* **755**, R5.
ROSSI, T. & TOIVANEN, J. 1999 A parallel fast direct solver for block tridiagonal systems with separable matrices of arbitrary dimension. *SIAM J. Sci. Comput.* **20** (5), 1778–1793.
ROWE, K.L., DIAMESSIS, P.J. & ZHOU, Q. 2020 Internal gravity wave radiation from a stratified turbulent wake. *J. Fluid Mech.* **888**, A25.
SPEDDING, G.R. 1997 The evolution of initially turbulent bluff-body wakes at high internal Froude number. *J. Fluid Mech.* **337**, 283–301.
SPEDDING, G.R., BROWAND, F.K. & FINCHAM, A.M. 1996 Turbulence, similarity scaling and vortex geometry in the wake of a towed sphere in a stably stratified fluid. *J. Fluid Mech.* **314**, 53–103.

DE STADLER, M.B. & SARKAR, S. 2012 Simulation of a propelled wake with moderate excess momentum in a stratified fluid. *J. Fluid Mech.* **692**, 28–52.

STRANDENES, H., JIANG, F., PETTERSEN, B. & ANDERSSON, H.I. 2019 Near-wake of an inclined 6: 1 spheroid at Reynolds number 4000. *AIAA J.* **57** (4), 1364–1372.

WIKSTRÖM, N., SVENNBERG, U., ALIN, N. & FUREBY, C. 2004 Large eddy simulation of the flow around an inclined prolate spheroid. *J. Turbul.* **5** (1), 029.

YANG, J. & BALARAS, E. 2006 An embedded-boundary formulation for large-eddy simulation of turbulent flows interacting with moving boundaries. *J. Comput. Phys.* **215** (1), 12–40.

ZHOU, Q. & DIAMESSIS, P.J. 2019 Large-scale characteristics of stratified wake turbulence at varying Reynolds number. *Phys. Rev. Fluids* **4** (8), 084802.